Spectral element modeling of seismic wave propagation in visco-elastoplastic media including excess-pore pressure development

Elif Oral[1,2], Céline Gélis[1], Luis Fabián Bonilla[2] and Elise Delavaud[1]

[1]Institut Radioprotection Sûreté Nucléaire, Fontenay-aux-Roses, France
[2]Université Paris Est - IFSTTAR, Marne-la-Vallé, France

Abstract

Numerical modeling of seismic wave propagation, considering soil nonlinearity, has become a major topic in seismic hazard studies when strong shaking is involved under particular soil conditions. Indeed, when strong ground motion propagates in saturated soils, pore pressure is another important parameter to take into account when successive phases of contractive and dilatant soil behavior are expected. Here, we model one-dimensional (1D) seismic wave propagation in linear and nonlinear media using the spectral element numerical method. The study uses a three-component (3C) nonlinear rheology and includes pore-pressure excess. The 1D-3C model is used to study the 1987 Superstition Hills earthquake (M_L 6.6), which was recorded at the Wildlife Refuge Liquefaction Array, USA. The data of this event present strong soil nonlinearity involving pore-pressure effects. The ground motion is numerically modeled for different assumptions on soil rheology and input motion (1C vs 3C), using the recorded borehole signals as input motion. The computed acceleration-time histories show low frequency amplification and strong high frequency damping due to the development of pore pressure in one of the soil layers. Furthermore, the soil is found to be more nonlinear and more dilatant under triaxial loading compared to the classical 1C analysis, and significant differences in surface displacements are observed between the 1C and 3C approaches. This study contributes to identify and understand the dominant phenomena occurring in superficial layers, depending on local soil properties and input motions, conditions relevant for site-specific studies.

Keywords: Seismic wave propagation, soil nonlinearity, cyclic mobility, viscoelasticity, spectral element method.

1 Introduction

In the last decades, local site conditions have emerged as one of the main components that govern the seismic ground motion. Numerous studies have shown that the ground response at a specific site is strongly controlled by the local soil properties, like the impedance contrast

between the bedrock and overlying layers (e.g. Kramer, 1996), constitutive material model and incident motion complexity (e.g. Gélis and Bonilla, 2012; 2014), and site geometry (e.g. Graves, 1993; Moczo et al., 1996 1996; Olsen and Archuleta, 1996).

Laboratory experiments performing cyclic loading on soil samples have shown shear modulus degradation and increasing damping for increasing shear deformation (e.g. Seed and Idriss, 1969; Vucetic and Dobry, 1991; Darendeli, 2001). This means reduction of the wave speed and increase of the energy dissipation of the propagation media, respectively. In addition, results from laboratory tests, involving pore-pressure measurements on cohesionless saturated soils, exhibit contractive and dilatant behavior; phenomena related to flow liquefaction and cyclic mobility (Ishihara, 1996).

Furthermore, many observations from past earthquakes, for example, the 1994 Northridge, 1995 Hyogo-Ken Nanbu (Kobe), 1999 Chi Chi, 2000 Tottori, 2011 Tohoku and 2015 Gorkha (Nepal) earthquakes show that nonlinear soil response is pervasive during strong motion (Aguirre and Irikura, 1997; Field et al., 1997; Roumelioti and Beresnev, 2003; Kokusho, 2004; Pavlenko and Irikura, 2003; Bonilla et al., 2011, Rajaure et al., 2016). In particular, in the presence of cohesionless saturated material having predominant dilatant behavior, observed accelerograms present high-frequency spiky waveforms leading to large acceleration pulses (Iai et al., 1995; Bonilla et al., 2005; Bonilla et al., 2011; Laurendeau et al., 2016).

Numerical modeling is an efficient tool to highlight the influence of different parameters governing site effects. Traditionally, nonlinear soil behavior has been approximated by the equivalent linear method (Schnabel et al., 1972). This method has widely been used because only the shear modulus and damping curves as a function of shear strain are needed and low computational effort is required (Bardet et al., 2000; Kausel and Assimaki, 2002). However, for strong input motion, the equivalent linear method is found to overestimate the material strength (Joyner and Chen, 1975; Yoshida and Iai, 1998; Hartzell et al., 2004; Stewart et al., 2008; Kaklamanos et al., 2015). Conversely, nonlinear soil constitutive models, based on the stress-strain history of cyclic behavior, have successfully been applied to one-dimensional (1D) wave propagation (Lee and Finn, 1978; Pyke, 2000; Hashash and Park, 2001; Bonilla et al., 2005). There are also extensions to 3D nonlinear models (i.e. Mroz, 1967; Dafalias and Popov, 1977; Prevost, 1977; Wang, 1990). Yet, many of these multi-dimensional models are based on numerous parameters, making their use sometimes prohibitive. The Masing-Prandtl-Ishlinskii-Iwan (MPII) model of Iwan (1967) (as adopted in Joyner and Chen, 1975; Joyner, 1975; Gandomzadeh, 2011; Santisi d'Avila et al., 2012; and Pham, 2013) is an interesting alternative to model material nonlinearity. Modeling is done by a set of nested yield surfaces consisting of simple elastic springs and Coulomb friction elements. It requires only the shear modulus reduction as a function of shear strain, which is readily obtained from laboratory data or from the literature for a wide range of soil classes (Vucetic and Dobry, 1991; EPRI, 1993; Ishibashi and Zhang, 1993; Darendeli, 2001).

Another important aspect is the choice of the numerical method to solve the wave equation. It influences the computational efficiency of numerical modeling in terms of precision of the solution and computational cost. One of the most commonly used methods to solve the seismic wave equation is the finite differences method (FDM), which has been extensively developed by many researchers (Madariaga, 1976; Virieux, 1986; Levander, 1988; Graves, 1996; Saenger et

al., 2000; Moczo et al., 2002). Soil nonlinearity has been modeled in several studies of 1D/2D seismic wave propagation using FDM with no pore pressure effects, also known as total stress analysis (i.e. Joyner 1975; Joyner and Chen, 1975; Gélis and Bonilla, 2012, 2014). Yet, FDM has also proven to be robust when pore pressure is taken into account. This kind of analyses are known as effective stress analysis and they are the only ones capable of modeling observed accelerograms strongly affected by dilatant/contractive soil behavior (i.e. Pyke, 2000; Bonilla et al. 2005). Although its implementation is relatively straightforward, FDM can present some limitations in modeling non-planar topographies or complex interfaces inside the medium.

A different approach, which facilitates the adaptation of mesh to complex geometries in 3D, is the finite element method (FEM) (Lysmer and Drake, 1972; Marfurt, 1984; Bielak et al., 2005). It has been used in many studies where nonlinear soil assumption is made for 1D - one-component (1C) and 1D - three-component (3C) seismic wave propagation (e.g. Iai et al., 1995; Hashash and Park, 2001; Borja et al., 2002; Gandomzadeh, 2011; Santisi d'Avila et al. 2012, 2011; Pham, 2013). However, one limitation of FEM is that the global mass matrix needs to be inverted at each time step, which results in longer computation times. Such heavy computations could be avoided by lumping the mass matrix to turn it into a diagonal matrix. Yet, such a procedure may introduce numerical dispersion (Hinton et al. 1976, Mullen and Belytschko, 1982, De Basabe and Sen, 2007). Combining different methods such as FDM and FEM has also been proposed (e.g. Moczo and Kristek, 2005; De Martin et al., 2007; Ducellier and Aochi, 2012).

As a promising alternative technique, the discontinuous Galerkin finite element method (DGM), based on exchange of numerical fluxes between adjacent elements, provides high order direct solution (Käser and Dumbser, 2006; Delcourte et al., 2009; Etienne et al., 2010; Peyrusse et al., 2014). Recently, DGM has been used in 1D wave propagation modeling in nonlinear media (e.g. Mercerat and Glinsky, 2015; Mercerat et al., 2016 and Régnier et al., 2016).

Another high-order finite element method is the spectral element method (SEM). It has been used in Geophysics for many years for seismic wave propagation modeling (Faccioli et al., 1997; Komatitsch and Vilotte, 1998; Seriani, 1998; Ampuero, 2002; Festa and Vilotte, 2005; Madariaga et al., 1976; Mercerat et al., 2006; Delavaud, 2007; Smerzini et al., 2011). It provides easiness of mesh adaptation to complex geometries with higher precision than finite differences and low-order finite element methods. Numerical algorithms of the spectral element method considering 1D and multi-dimensional plasticity theory have been used in engineering models (Leroy, 2011). Some recent studies using SEM for seismic wave propagation also take into account nonlinear soil behavior (i.e. Stupazzini and Zambelli, 2005; di Prisco et al., 2007; Stupazzini et al., 2009, He et al., 2016). Moreover, SEM was used in studies of seismic wave propagation in nonlinear crustal fault zones (Lyakhovsky et al., 2009; Xu et al., 2012; Gabriel et al., 2013; Xu et al., 2015 and Thomas et al., 2017).

In this work, we develop a numerical tool to study soil nonlinearity respecting geomechanical characteristics of the medium and considering the excess-pore pressure development effects on soil behavior. We exploit the numerical advantages of SEM regarding precision and mesh adaptability to various medium properties. This advantage provides relatively cheaper computational times compared to other numerical methods having higher number of elements reaching the same accuracy (De Martin, 2010). As for the nonlinear soil constitutive model, we use MPII

model of Iwan (1967). In this approach, the total material damping is modeled through a combination of viscoelasticity and hysteretic behavior as suggested by Assimaki et al. (2011) and Gélis and Bonilla (2012, 2014). For the purpose of modeling pore-pressure effects, we follow the formulation of Iai et al. (1990), which relates pore-pressure changes to the cumulative shear work (total shearing) produced during wave propagation. This empirical relation needs several parameters that can be obtained in the laboratory data or earthquake inversion analyses (Iai et al., 1990; Iai et al., 1995; Bonilla et al., 2005; Roten et al., 2013; 2014).

In this paper, we first present the 1D-3C SEM code development. We then show the verification using the nonlinear and viscoelastic rheologies for 1C shear wave propagation by reproducing the computations performed in the PRENOLIN project (Mercerat et al., 2016; Régnier et al., 2016) and in previous studies (Peyrusse et al., 2014; Martino et al., 2015). Secondly, we study the impact of taking into account the multi-component wave propagation on the development of soil nonlinearity compared to the traditional 1C analysis. Lastly, we model the acceleration-time histories of the 1987 Superstition Hills earthquake recorded at the Wildlife Refuge Liquefaction Array (WRLA). A sensitivity analysis is performed to assess the influence of soil rheology and the number of components propagating in the 1D medium (1C vs 3C) for the same site.

2 Numerical Scheme and Constitutive Models

In this section, the spectral element method is briefly presented. Then, the constitutive models are given for viscoelasticity and nonlinearity of the medium.

The spectral element approximation is based on the decomposition of the domain into overlapping elements Ω_e (segments in 1D, quadrangles in 2D and hexahedra in 3D). In each element Ω_e, Gauss-Lebatto-Legendre (GLL) integration points are defined. Lagrange polynomials are then chosen to define an orthogonal basis, which enables the SEM to have a spectral convergence, making it a very precise numerical method (Festa and Vilotte, 2005; Delavaud, 2007). In our case, the equation of wave propagation follows the velocity-stress formulation. The time discretization follows the leap-frog scheme. The time step has to verify the Courant-Friedrichs-Lewy (CFL) condition to ensure the stability of this time-marching solver. We use 0.3 as the controlling value of CFL for all the applications in this paper. Here the definition of the controlling value is adopted from Delavaud (2007), in which the computed CFL number is based on minimum spacing between GLL nodes in the spectral element. The element size d is chosen by respecting the formula $d \leq \lambda_{min} N/ppw$, where λ_{min} is the shortest wavelength propagating in the medium, N is the polynomial degree and ppw is the number of grid points per wavelength, to avoid artificial wave dispersion (Seriani and Priolo, 1991). In the aforementioned study, the authors show that the use of $ppw = 5$ is needed for a wave propagation without numerical dispersion, while finite difference and low-order finite element methods require values between 15 and 30.

The 1D-3C nonlinear SEM code has built-in different soil rheologies such as linear, viscoelastic and visco-elastoplastic behavior. In a viscoelastic medium, attenuation is quantified by using the quality factor Q (Aki and Richards, 2002; Moczo and Kristek, 2005). The convolu-

tion relating stress and strain in the frequency domain in viscoelasticity theory is converted into a differential form by means of additional memory variables to model the viscoelastic attenuation, corresponding to a Generalized Maxwell Body (Day and Minster, 1984; Emmerich and Korn, 1987; Day and Bradley, 2001). In this study, we choose the approach proposed by Liu and Archuleta (2006) that approximates a constant Q between 0.01 and 50 Hz by eight mechanisms of pre-calculated memory variables. In the 1D-3C SEM code, the memory variables and the viscous modulus corresponding to Q_p and Q_s values at a given reference frequency f_r are utilized, respectively. We recall that the total energy dissipation in the soil is modeled as the sum of viscoelastic attenuation and hysteretic attenuation similarly to Assimaki et al. (2011) and Gélis and Bonilla (2012; 2014).

Soil nonlinearity follows the hyperbolic model proposed by Hardin and Drnevich (1972) (the reader can find the details in that paper). Equation (1) shows the relation between shear modulus G and shear strain γ for this model, where G_0 is the initial shear modulus and γ_{ref} is the reference shear strain defined as the ratio between the shear strength and the initial shear modulus.

$$\frac{G}{G_0} = \frac{1}{1 + \gamma/\gamma_{ref}} \tag{1}$$

The MPII model (Iwan, 1967) (described in Appendix A.1) uses these hyperbolic curves to construct the stress-strain space in 3D. Our code follows Joyner's formulation (1975). The matrix of total-stress increment corresponding to a given matrix of strain increment is calculated based on parameters of deviatoric stress and strain.

To model the excess-pore pressure generation under cyclic loading we follow the study of Iai et al. (1990). In their study, the authors relate the cumulative shear work and the mean effective stress as it has been observed in experimental data (Towhata and Ishihara, 1985). The time evolution of the parameters in this relation is called liquefaction front. The liquefaction front represents the envelope of stress points at equal shear work in normalized stress space relating the applied normalized deviatoric stress r to current normalized mean effective stress S (the normalization factor is the initial mean effective stress). In this stress plan, the soil is characterized by two limits during cyclic loading. The first one is the transition between contractive and dilatant behaviors and the second one is the rupture limit. The boundaries of these two limits are called phase transformation and failure lines, respectively (Figure 1). The 1D-3C SEM code couples the nonlinear MPII model with the model of Iai et al. (1990) in presence of liquefiable soil layers. At each time step, the increment of the cumulative plastic shear work and the current effective stress corresponding to the matrix of current total stress are computed. The backbone curve of the soil (hyperbolic curve of Equation 1) is reconstructed according to the current effective stress. Appendix A.2 describes all equations and parameters related to the liquefaction front model.

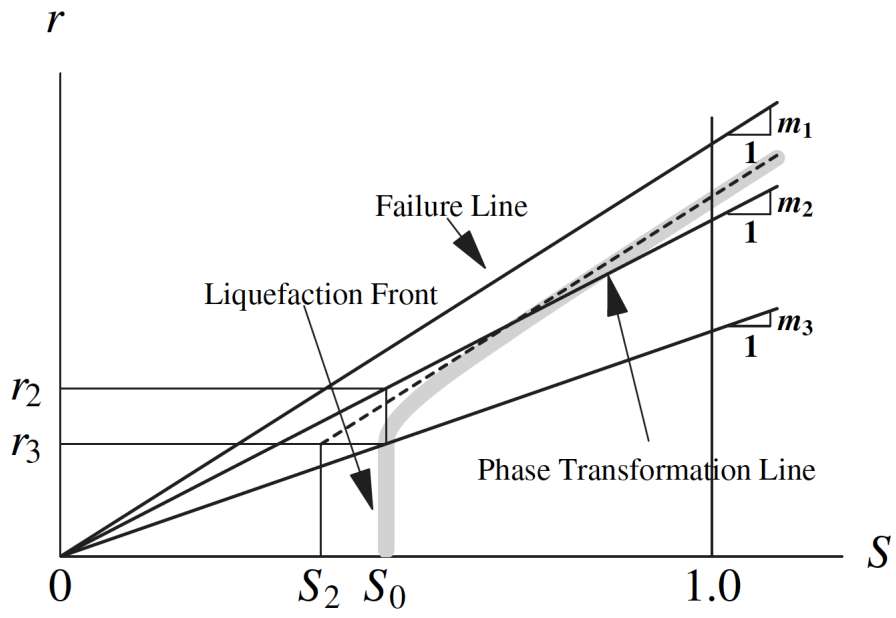

Figure 1: Schematic plot of liquefaction front model in normalized stress space. S holds for normalized mean effective stress and r is the normalized deviatoric stress (after Iai et al., 1990).

The medium is divided into elements for the wave propagation modeling. The mesh for a nonlinear medium is created based on the shortest wavelength. Since we do not have an adaptive meshing in time and space, the procedure we follow is to suppose that the minimum shear wave velocity during the simulation does not become less than one-fourth of the initial shear wave velocity (corresponding to the reduction of shear modulus to one-sixteenth of the initial shear modulus). We check at the end of the simulation whether the computed strains are compatible with the a priori shear modulus reduction to see if the solution is stable (e.g. Gélis and Bonilla, 2012). If the minimum shear modulus during the simulation becomes less than one-sixteenth of the initial shear modulus, we further refine the meshing by a factor of 2. For all the nonlinear models in this study, 50 springs of MPII model are used. In Appendix B, the influence of number of GLL nodes and Iwan springs on the precision of SEM solution in nonlinear media is shown for one of the models used in this paper.

3 Verification of viscoelastic and nonlinear modeling

Different tests are performed to compare SEM results with other numerical methods for the purpose of verification. First, the verification of viscoelasticity implementation is performed followed by the one considering nonlinear rheology. The wave propagation is computed using only one shear component in both cases.

To verify the viscoelasticity implementation, we perform 1D-3C SEM computations of a soil profile in Rome, Italy from Martino et al. (2015) study. We then compare these results

with those used in Martino et al. (2015). The 1D Rome model is composed of 14 soil layers overlying bedrock (Table 1). The soil profile includes velocity inversions, for example layer 4 has a higher velocity than layer 5. The reference frequency f_r is set to 1 Hz for all layers. Such a complex model allows to track small differences between numerical methods up to high frequencies. The free surface is modeled by a Neumann condition. Elastic rock boundary at bottom is modeled by absorbing layers of Classical Perfectly Matched Layers (C-PML). The input motion used is the same as in Peyrusse et al. (2014), a synthetic Gaussian wavelet low pass filtered below 14 Hz. The velocity-time history and corresponding Fourier amplitude of the input motion (after filtering) are shown in Figure 2. A mesh corresponding to a resolution of 20 Hz and a 4th polynomial order (5 GLL points per element) is used. The element size varies from 2.5 to 16 m and a maximum number of two elements are used on each layer. Minimum distance between GLL points of elements changes from 0.4375 to 2.8 m. The time step is set to 2 x 10^{-5} s. The source is located at a depth of 100 m. In Figure 3, acceleration-time histories at the surface from SEM and the Haskell-Thomson (HT) methods are shown in the top panel. Both techniques give identical results, verifying the implementation of the attenuation in the time-domain computations. The lower panel of Figure 3 shows the transfer functions obtained by SEM and HT. They are obtained by computing the spectral ratio (FFT) of surface with respect to input motions. Since the input energy is limited to 14 Hz, the results are shown up to this frequency limit. Given the complexity of the media, this good agreement between the results of all the methods demonstrates the correct implementation of viscoelasticity. Appendix C.1 addresses the goodness-of-fit of these simulations.

Table 1: Soil properties at the Rome model.

Layer	Thickness $[m]$	$V_s[m/s]$	$V_p[m/s]$	$\rho[kg/m^3]$	Q_s	Q_p
1	10	220	490	1835	100	200
2	6	239	523	1876	15	30
3	16	260	1480	1967	100	200
4	13.5	417	1760	1957	50	100
5	10	212.5	1235	1865	35	70
6	2.5	417	1760	1957	50	100
7	7	713	2560	2141	50	100
8	3	545	2125	2078	35	70
9	2.5	610	2379	2078	35	70
10	3	675	2632.5	2078	35	70
11	2.5	740	2886	2078	35	70
12	3	805	3139.5	2078	5000	10000
13	2.5	870	3393	2078	5000	10000
14	2.5	935	3646.5	2078	5000	10000
Bedrock	16	1000	3900	2078	5000	10000

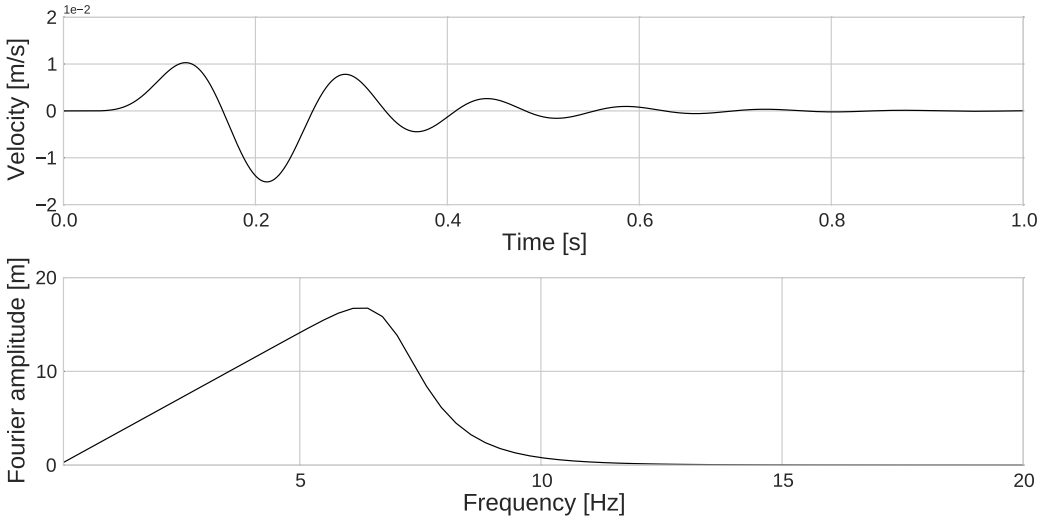

Figure 2: Velocity-time history (top) and Fourier amplitude (bottom) of the input motion used in Rome soil profile.

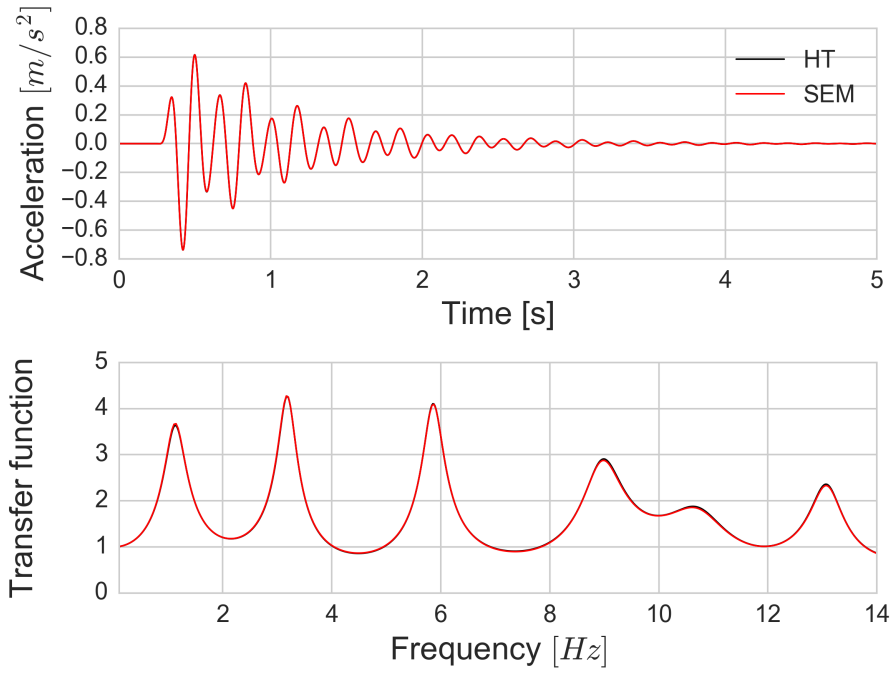

Figure 3: Comparison between acceleration-time histories at surface from SEM (in red) and HT (in black) (top) and transfer functions obtained with SEM (in red) and HT (in black) (bottom).

To verify the implementation of the nonlinear soil model, we use one of the results obtained within the PRENOLIN project (Régnier et al., 2016). This project aims at comparing 1D numerical wave propagation codes, having 21 international participating teams to model soil nonlinearity using canonical and real cases. One of the canonical cases of the project, the so-called P1 model, is used in this verification test. The free surface is modeled by a Neumann

condition. At the bottom of the model, the rigid boundary is modeled by a Dirichlet condition with a zero velocity-field. In the P1 model, a single layer of soil is defined with a thickness of 20 m and a velocity of 300 m/s overlying a bedrock having a shear velocity of 1000 m/s. A fourth-order polynomial degree (5 GLL points) is chosen for this model. A simple Ricker signal with a PGA of 0.93 m/s^2 and a duration of 1 s, provided by the project, is imposed as input motion at the bottom of the discretized domain. In order to remove potential numerical noise with minimal loss of signal components, an acausal low-pass filtering is applied below 10 Hz by using a Butterworth filter before and after the simulation. The time step is set to 5 x 10^{-5} s. Elements of 5 m size are used in the model. The results obtained with SEM are compared to the results of another participant of the project, team EY, (Mercerat and Glinsky, 2015; Régnier et al., 2016), who uses discontinuous Galerkin method (DGM) code, where the MPII model is also implemented. Figure 4 shows the stress-strain diagram for the point located at GL-9 m (left). Both methods show similar dynamic loading paths with negligible differences at the extreme values. Furthermore, due to soil nonlinearity, the material behavior is no longer elastic and experienced values of shear strain become significant even under such simple input and site conditions.

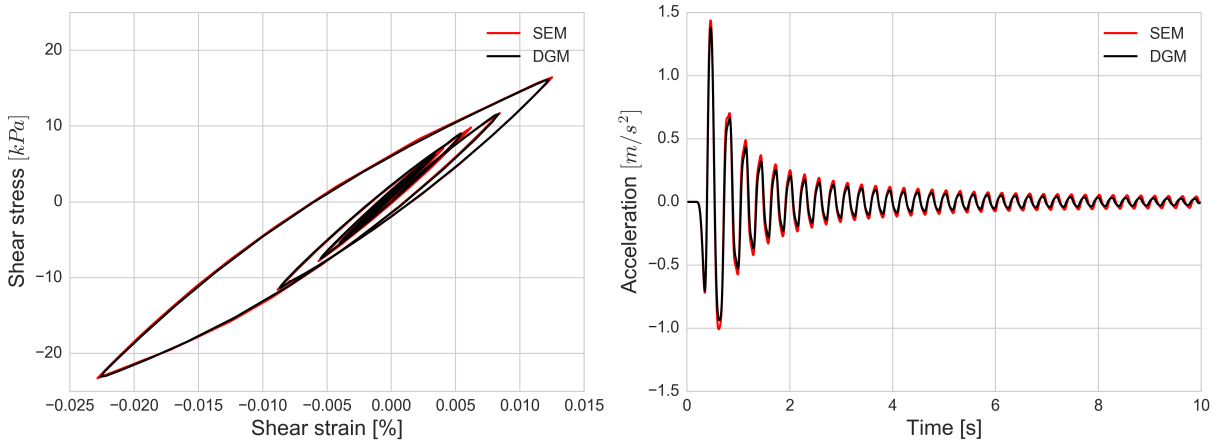

Figure 4: Stress-strain curves computed with SEM (in red) and DGM (in black) for the P1 model simulation using elastoplastic behavior (left). Acceleration-time histories at the surface computed with SEM (in red) and DGM (in black) (right).

Another comparison between two methods is made on the computed time histories of surface acceleration, Figure 4 (right). SEM results show slightly higher peak acceleration amplitudes than DGM, which could be related to possible differences between SEM and DGM numerical modeling. Yet, the results obtained with the two methods are in good agreement in terms of waveform and phase. Appendix C.2 quantifies the similarity of these two simulations. Other comparisons between different numerical schemes using Iwan (1967) nonlinear model in 1D seismic wave propagation can be found in Mercerat et al. (2016).

4 Comparison of uniaxial and triaxial loading

In the 1D-3C SEM code, the propagation can be computed using two shear components (x,y) and one compression component through the vertical axis (z), so that all the three components (x, y, z) can be considered in the calculations. Under multi-axial stress state, the loading is likely to lead to more energy dissipation and to result in a consequent plastification effect in the soil (Santisi d'Avila et al., 2012). In this section, we compare the nonlinear soil behavior under uniaxial and triaxial loading without modeling pore-pressure excess. For this purpose, the previously used P1 model is used with the same input signal. The soil column is loaded in the x-direction only, so that the propagation is done for one shear component. For the triaxial loading, the same input signal is defined for all components (x, y, z). This configuration is not realistic, but it is only used for demonstration purposes. Figure 5 (left) shows that the stress-strain curve at the middle of the soil follows the prescribed backbone curve under uniaxial loading; while the right figure shows that the soil deviates from the backbone curve under triaxial loading. Such behavior indicates higher plastification that leads to loss of soil strength and change in deformation values in the soil with higher damping. Consequently, at the surface, resultant motion is stronger for uniaxial loading than triaxial loading (top panel of Figure 6). From the initial seconds of simulation, the increase in attenuation is noticeable.

Furthermore, a slight time shift of multi-component simulation with respect to one-component computation is observed. Such an outcome is a consequence of higher nonlinearity corresponding to a lower shear modulus (lower wave speed) under triaxial loading. The transfer functions illustrate the impact of this higher nonlinearity under triaxial loading showing larger attenuation of maximum values (bottom panel of Figure 6). The fundamental frequency is also slightly shifted from 3.5 Hz to 3.4 Hz.

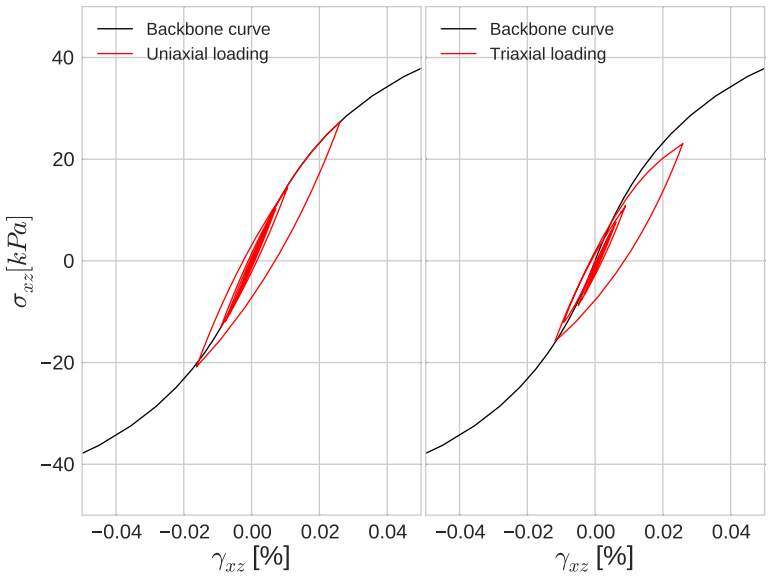

Figure 5: Comparison of the stress-strain curves for the P1 soil model under uniaxial (left) and triaxial loading (right). The backbone curve is shown in black.

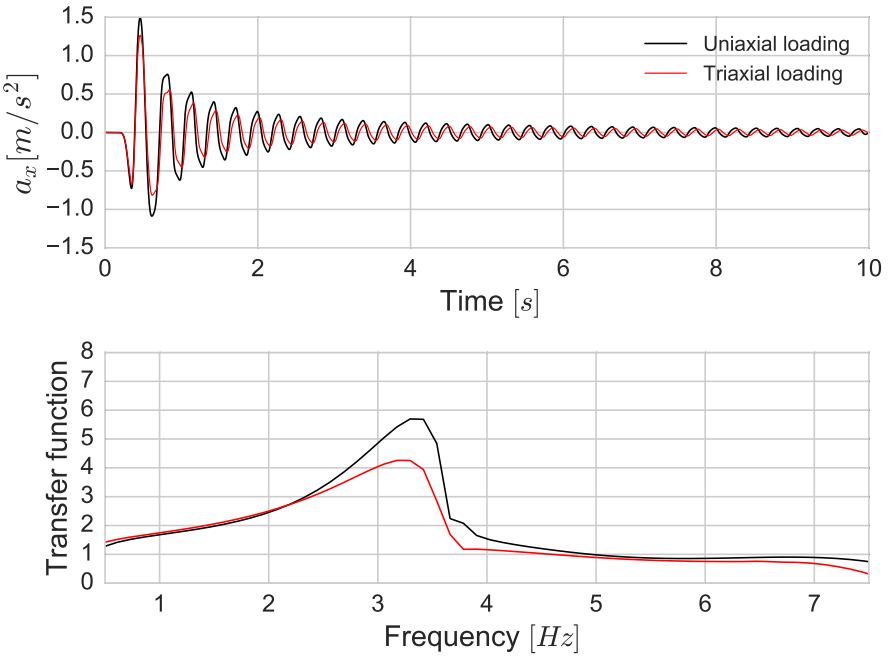

Figure 6: Surface acceleration-time histories (top) and transfer functions (bottom) for uniaxial (in black) and triaxial loading (in red).

The fact that soil becomes more plastic due to multiaxial loading even in cases where propagation is modeled for simple input motion shows the coupling of motion components in a 3D nonlinear constitutive soil model. In more realistic conditions of input loading, plasticity arises mostly from double shearing because the horizontal components of the ground motion are usually larger than the vertical one. Yet, this can be a critical issue in the vicinity of the source where the vertical component may also be equal or larger than the horizontal ones. For this reason, additional energy attenuation with higher nonlinearity due to multiaxial loading should be taken into account for realistic modeling of seismic wave propagation.

5 Validation of the 1D-3C SEM code including pore-pressure effects

5.1 The 1987 Superstition Hills Earthquake

To validate the 1D-3C approach, we use data recorded at the Wildlife Refuge Liquefaction Array (WRLA), located on the floodplain of Alamo River in the Imperial Valley of California. The array was deployed by the United States Geological Survey (USGS) in 1987 with surface and downhole accelerometers (GL-7.5 m) and pore-pressure transducers at different depths. At WRLA, the pore-pressure changes were recorded together with the seismic motion generated by the M_L 6.6 mainshock of Superstition Hills on the 24 November 1987 (Holzer et al., 1989).

We adopt the parameters of Bonilla et al. (2005) for the soil properties in our study. The velocity profile is composed of 4 soil layers as seen in Table 2. V_s and V_p correspond to shear

and pressure wave velocities, respectively; ρ is the density, ϕ_f is the friction angle representing the failure line, and K_0 is the coefficient of Earth at rest needed to compute the initial stress conditions. The water table depth is set to 2 m. The site is assumed to be initially isotropically consolidated and dilatancy parameters (ϕ_p, w_1, p_1, p_2 and S_1) are used for the third layer as proposed by Bonilla et al. (2005).

Table 2: Soil properties at Wildlife Refuge Liquefaction Array after Bonilla et al. (2005).

Layer	Description	Thickness $[m]$	$V_s[m/s]$	$V_p[m/s]$	$\rho[kg/m^3]$	$\phi_f[degree]$	K_0
1	Silt	1.5	99	249	1600	28	1.0
2	Silt	1.0	99	281	1928	28	1.0
3	Silty sand	4.3	116	1019	2000	32	1.0
4	Silty sand	0.7	116	1591	2000	32	1.0

Table 3: Dilatancy parameters for the loose silty sand layer at the Wildlife Refuge Liquefaction Array (after Bonilla et al., 2005).

$\phi_p[degree]$	w_1	p_1	p_2	S_1
24.0	4.0	0.4	0.9	0.01

5.2 Numerical model

Borehole wavefield at GL-7.5 m depth is used as input in the simulations. The strongest motion is recorded on the north-south direction with an amplitude of 1.60 m/s^2, while the weakest motion is on the vertical direction with a PGA of 0.54 m/s^2, Figure 7. Hereafter, north-south component is symbolized by (NS), east-west component by (EW) and vertical component by (UD).

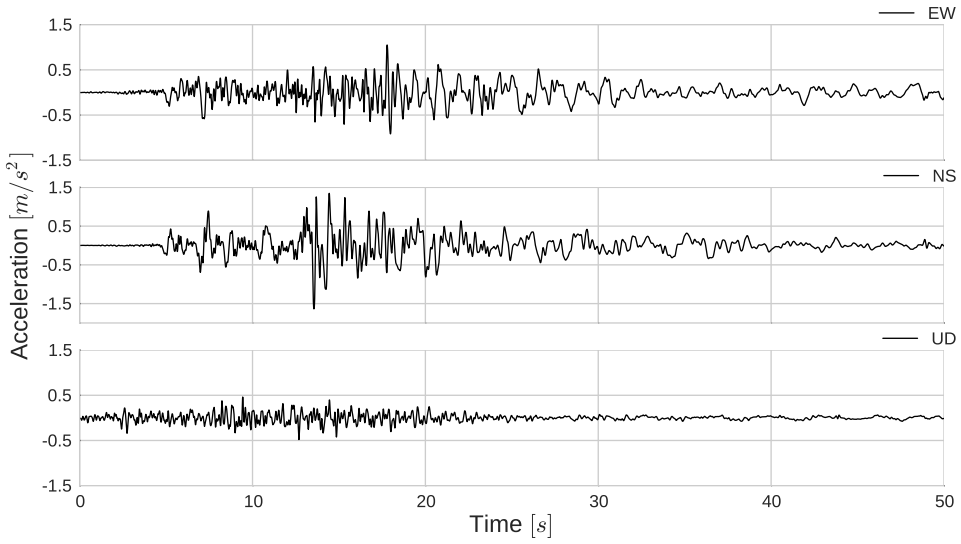

Figure 7: Acceleration-time histories recorded in the east-west (EW), north-south (NS) and vertical (UD) directions at GL-7.5 m depth of WRLA.

The computation is done for a resolution up to 10 Hz where the minimum grid spacing is 0.5 m, each spectral element has 5 GLL points and time step Δt = 1.0 x 10^{-5} s. The quality factors for shear and pressure waves are taken as $V_s/10$ and $V_p/10$, respectively. For all the defined integration points in the model, the reference strain γ_{ref} is computed by Equation (2), so that reference strain is not the same all over the domain but proportional to vertical confining stress.

$$\gamma_{ref} = \frac{sin\phi_f * \sigma'}{G} \tag{2}$$

where ϕ_f is the failure line angle, σ' is the initial effective stress and G is the corrected shear modulus used in the simulations (initial shear modulus multiplied by a coefficient of $(\frac{\sigma'}{\sigma'_{mid}})^{0.5}$ where σ'_{mid} is initial effective stress at the middle of the layer) defined for each GLL point. Shear modulus is pressure-dependent, which means that soil is more linear at depth and more nonlinear close to surface.

5.3 Results

We compare the observed ground motion at the surface with the computed synthetics in the three directions. Figure 8 shows the computed accelerations at the surface. After the first 13 s, the accelerograms show large dilatation pulses riding on a low-frequency carrier. Except for the slight phase differences on the NS component and some amplitude dissimilarities, the simulation is able to reproduce well the observed ground motion.

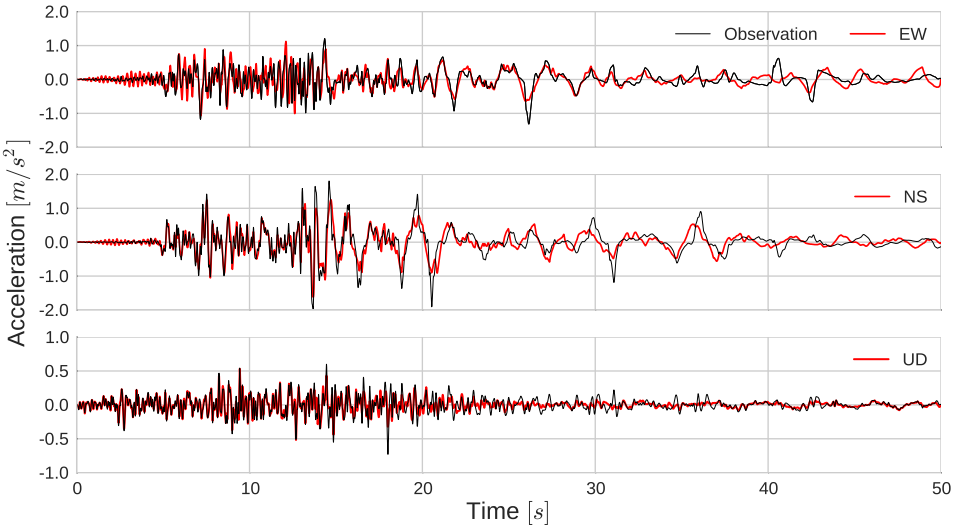

Figure 8: Comparison of surface acceleration-time histories between the results of effective stress analysis of SEM (in red) and real records (in black) for the WRLA site.

Moreover, a similar comparison is made between computed and observed velocity-time histories, Figure 9. After 20 s, SEM solution and observation on the NS component exhibit slight phase and amplitude differences. Appendix C.3 shows the goodness-of-fit analyses of SEM results with respect to observed acceleration and velocity-time histories, respectively.

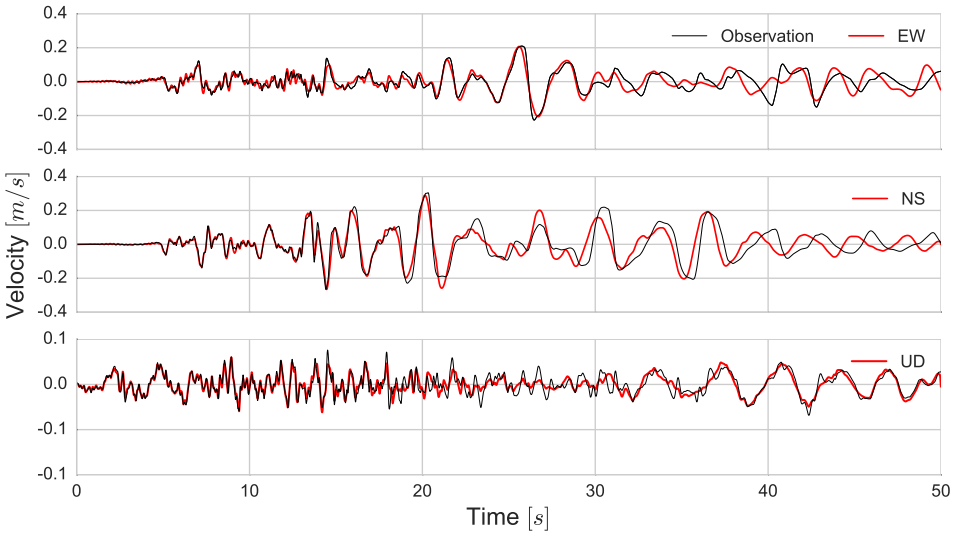

Figure 9: Comparison of surface velocity-time histories between the results of effective stress analysis of SEM (in red) and real records (in black) for the WRLA site.

The long period pulses in the horizontal components of the acceleration-time histories can be explained by the dilatancy changes in the liquefiable silty sand layer (GL-2.5 m - GL-6.8

m). Two points at different depths are chosen to see these changes. The first corresponds to a depth of GL-2.9 m, where pore pressure effects were recorded; and the second is located in the middle of the soil column. Figure 10 shows the normalized deviatoric stress (r) as a function of the normalized current effective stress (S) for these two points (initial effective stress is used as normalization factor). A continuous decrease in effective stress is observed. At GL-4.0 m depth, the soil experiences dilatant behavior by reaching the phase transformation line.

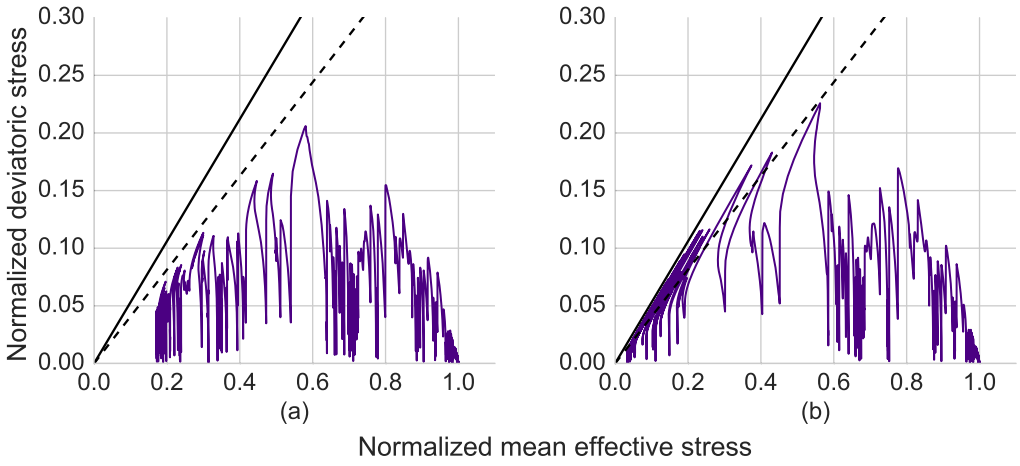

Figure 10: Stress space at GL-2.9 m (a) and GL-4.0 m (b), respectively. Solid and dashed lines represent the failure and phase transformation boundaries.

Moreover, the stress-strain curves are plotted for the same locations in Figures 11-12. At each depth, the decrease in effective confining stress can be remarked by slope changes of shear strength. Differently than GL-2.9 m, dilatancy at GL-4.0 m results in stress-strain loops for shear components having the classical banana shape, which is typical of softening and partial regain of soil strength due to successive changes in soil dilatancy. Maximum strain reached by the soil at this depth is close to 5 %. Strain values at depth GL-2.9 m are small due to the large attenuation of the incoming waves. Conversely,in the vertical component at either depth, the behavior is close to elastic conditions. Such an outcome results from the fact that the bulk modulus is independent of soil dilatancy changes in this model. Such an assumption should be studied in the future, yet it produces good results when modeling the vertical wave propagation in this case.

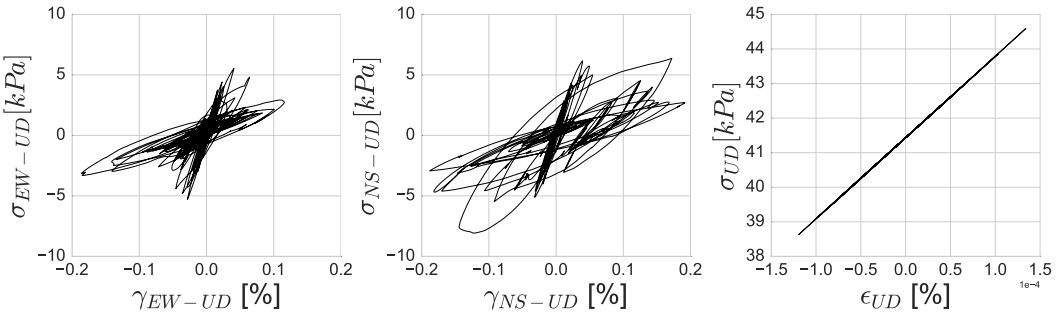

Figure 11: Stress-strain curves of EW-UD component (left), NS-UD component (middle) and UD component (right) at GL-2.9 m.

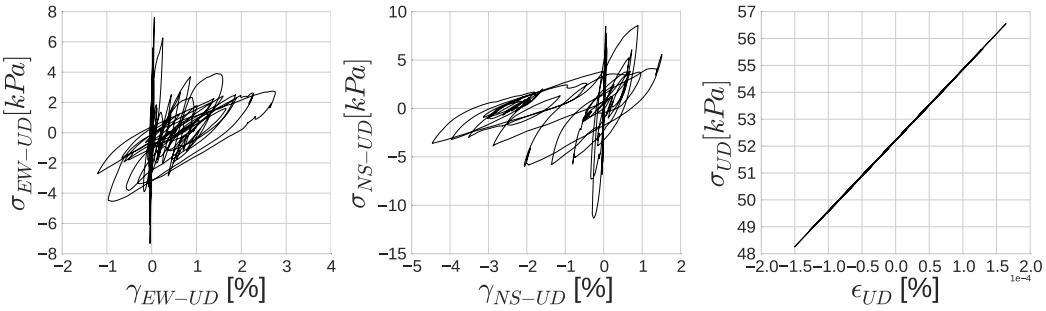

Figure 12: Stress-strain curves of EW-UD component (left), NS-UD component (middle) and UD component (right) at GL-4.0 m.

Furthermore, we compute the change of the pore-pressure excess inside the liquefiable soil layer. Figure 13 displays at GL-2.9 m (left) and those computed at GL-2.9 m and GL-4.0 m (right), respectively. A sudden increase in pore pressure is seen after 13 seconds at both depths. Since the effective stress decreases more at GL-4.0 m, the pore-pressure excess reaches higher values than GL-2.9 m. Continuous changes in contractive-dilatant behavior of the soil at GL-4.0 m is seen in the same figure by successive oscillations in pore-pressure values. As soil becomes contractive, pore pressure decreases, while it increases for dilatant soil behavior. Such sudden changes in dilatancy, where stress path changes direction and effective stress increases with dilatant behavior, are related to partial gain of strength and consequent spiky values in surface acceleration which take place after 13 s. Oscillations related to dilatant behavior at GL-2.9 m in SEM solution have higher amplitudes compared to the recording. Although these differences are not significant to interpret the evolution of soil behavior under excess-pore pressure development, the numerical solution could be improved by modification of parameters of the liquefaction front model. Indeed, the parameters used in this study have been determined for another constitutive model of soil nonlinearity (Iai et al., 1990; Bonilla et al., 2005). Also,

triaxial loading condition leads the soil to higher nonlinearity, differently than the mentioned studies that used uniaxial loading condition. Furthermore, in Holzer and Youd (2007), the authors explained the continuous increase in pore-pressure excess and ultimate liquefaction process with the formation of surface waves (Love and Rayleigh waves) and consequent shearing in WRLA. Same authors stated the presence of surface waves in the input motion at GL-7.5 m, which suggests the importance of 2D/3D effects on the incoming wavefield that may increase the pore-pressure effects. However, the generation and lateral propagation of these surface waves cannot be accounted for our 1D model.

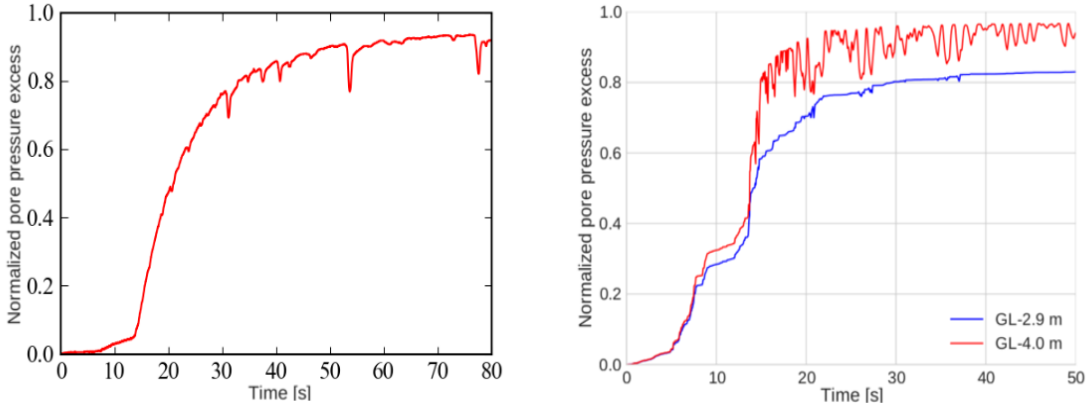

Figure 13: Pore-pressure ratio at GL-2.9 m (left) (extracted from Holzer and Youd, 2007 and modified after Pham, 2013). Computed pore-pressure ratios at GL-2.9 m (in blue) and at GL-4.0 m (in red), respectively (right).

Thus far, the influence of cyclic-mobility phenomenon in the 4.3 m thick silty sand layer is demonstrated and the spiky wavelets at surface are explained due to the sudden changes in pore pressure and dilatant behavior of the silty sand layer. The good agreement between observed and calculated accelerations supports the nonlinear soil rheology used in this study. In the next section, a sensitivity study is carried out to highlight the effect of soil rheology and input loading (1C and 3C approaches) at WRLA.

5.3.1 Influence of material rheology on wave propagation

We investigate the influence of ignoring the excess-pore pressure development on the response of the WRLA soil column using a visco-elastoplastic analysis. Three components of the computed acceleration-time histories at the surface are compared between two approaches (with/without pore-pressure effects). Figure 14 shows that signals are dominated by high-frequency motion in both shear components. The particular waveform observed after first 13 s in these components cannot be reproduced. Conversely, only few differences are noted between the calculated and observed vertical motions. Such an outcome arises from the fact that the constitutive equations lead to development of strong material nonlinearity mainly in the deviatoric plan. It is a drawback of the model since it will not be able to correctly model volumetric changes during cyclic loading. This aspect has to be improved in the future to

correctly predict vertical settlements.

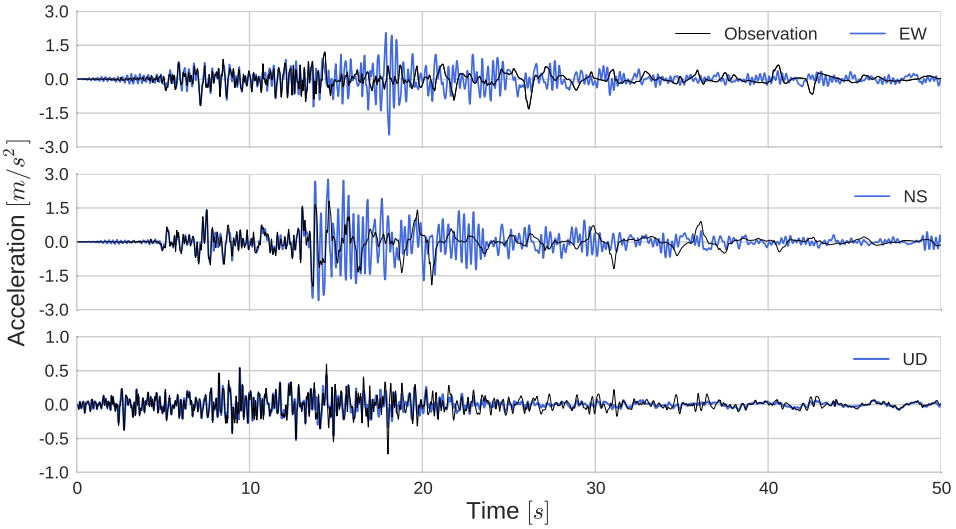

Figure 14: Surface acceleration-time histories for simulation without pore-pressure effects (in blue) and observation (in black) at the WRLA.

The effect of pore-pressure excess is also shown on the response spectra. Figure 15 depicts the 5 % response spectra of the three components of surface acceleration for effective stress analysis (in red) and total stress analysis (in blue). A very strong peak around 3 Hz in the visco-elastoplastic analysis without pore-pressure excess is noted in both shear directions. This peak is significantly damped with the introduction of cyclic mobility in the third layer so that the results become much closer to the observations. In addition, at low frequencies (< 1 Hz), the spectrum is amplified when excess-pore pressure is taken into account, which results in a better fit to the observation. As before, the vertical component remains unaffected by the presence or not of pore pressure.

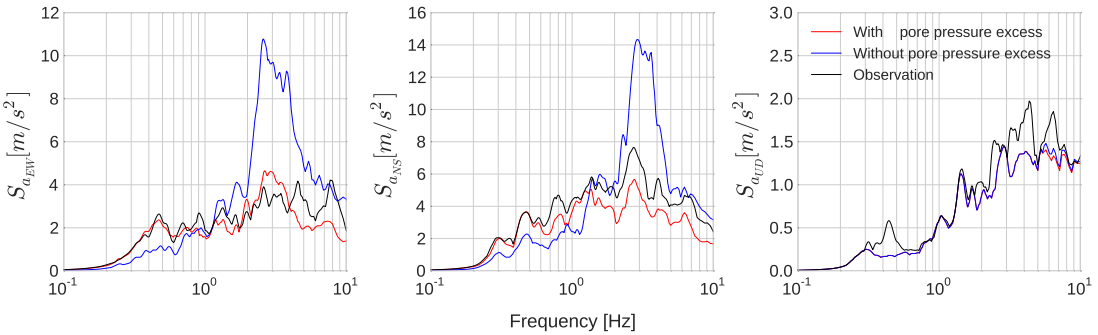

Figure 15: **Comparison of response spectra between real records (in black), effective stress analysis of SEM (in red) and total stress analysis of SEM (in blue) for EW component (left), NS component (middle) and UD component (right).**

These results reveal the importance of taking into account the correct soil constitutive model in surface-motion modeling. The response spectra of ground motion are strongly influenced by soil rheology in the frequency band of interest for Earthquake Engineering (0.1-10 Hz). Thus, for certain structures whose resonance frequencies fall into the low-frequency band, the design could exceed the safety limit if the rheological characteristics of the underlying media are not correctly taken into account. Such considerations enhance the importance of realistic hypothesis and good knowledge of the soil behavior and properties during site-specific studies.

Furthermore, the depth profiles of maximum strain for the three components of total and effective stress analyses are compared in Figure 16. A significant increase in strain values of the third layer is noted on the shear components for the simulation with excess-pore pressure development. The maximum soil strain reaches to 5 % on NS-UD component of shear strain (γ_{NS-UD}), while it does not exceed 0.2 % without pore-pressure excess. Concomitantly, as the strain increases in the third layer, an overall strain decrease is seen in other layers. In a highly nonlinear liquefiable soil layer, the incoming waves could be trapped under pore-pressure effects and such wave trapping could result in higher deformation in effective stress analysis compared to total stress analysis.

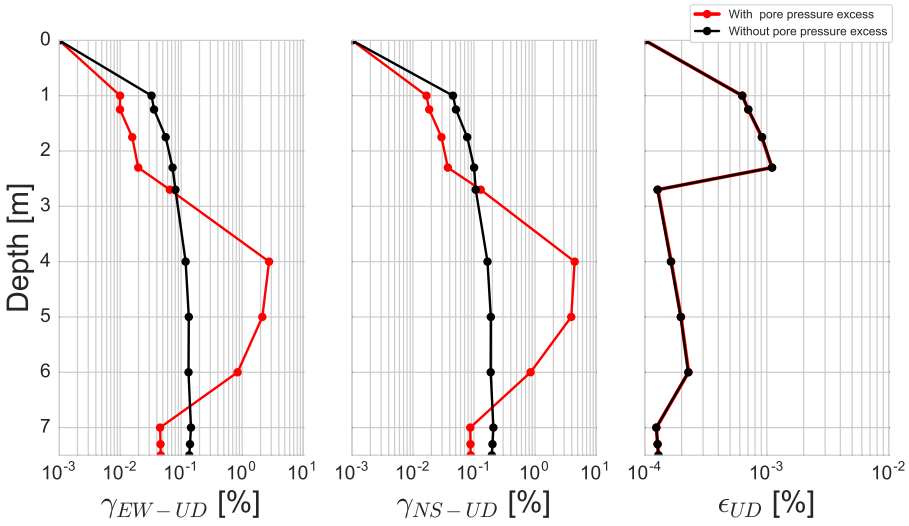

Figure 16: **Comparison of maximum strain profiles as a function of depth between effective stress analysis of SEM (in red) and total stress analysis of SEM (in black) for EW-UD (left), NS-UD (middle) and UD (right) components.**

5.3.2 Uniaxial vs Triaxial loading

Here, we compare the response of the soil column under uniaxial and triaxial loading conditions. In Section 4 we showed that the soil becomes more nonlinear due to multi-component loading. In this section, we investigate this effect in a real model, in which pore-pressure excess plays an important role, using the real records for the site. For this purpose, we propagate only the NS component in uniaxial loading case. The comparison is made in the direction where the motion is the strongest.

The results of acceleration, velocity and displacement time histories computed at the surface are shown in Figure 17. In the first 13 seconds, the results are very similar between uniaxial and triaxial loading. Then, waves arrive later in triaxial loading than uniaxial loading. This phase difference indicates that the velocity of the media has further decreased under triaxial loading. Indeed, soil behavior exhibits higher amplitudes and presents larger permanent displacements for the 3C computations compared to traditional 1C computations.

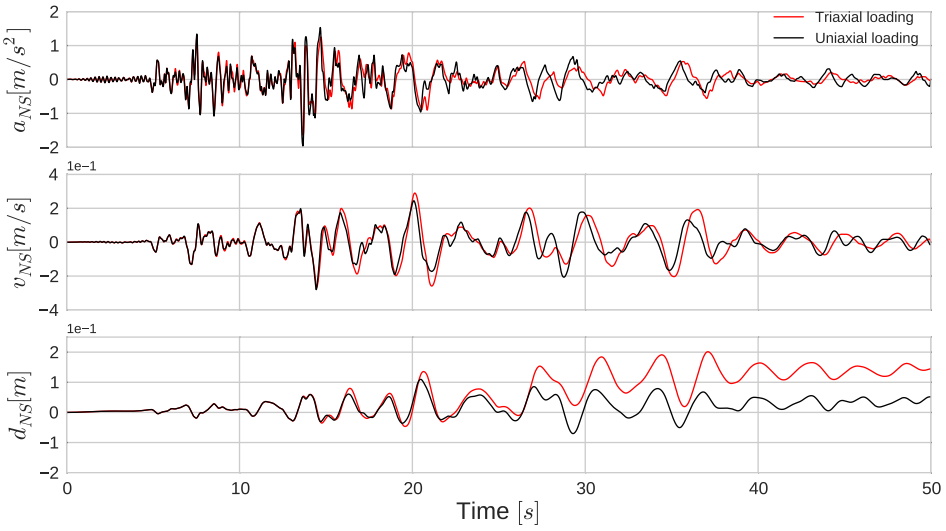

Figure 17: **Comparison of maximum strain profiles as a function of depth between effective stress analysis of SEM (in red) and total stress analysis of SEM (in black) for EW-UD (left), NS-UD (middle) and UD (right) components.**

Furthermore, the stress-strain loops at GL-4 m show more nonlinear and dilatant behavior, producing higher deformations during triaxial loading compared to uniaxial loading (Figure 18, left). Given the fact that soil is more nonlinear during triaxial loading, the effective stress decreases more rapidly resulting in earlier and stronger pore pressure rise. In consequence, the soil undergoes with more oscillations in the second half of the simulation (after 13 s) under triaxial loading (Figure 18, right). Therefore, multi-axial interaction may become important for a realistic analysis on seismic wave propagation studies.

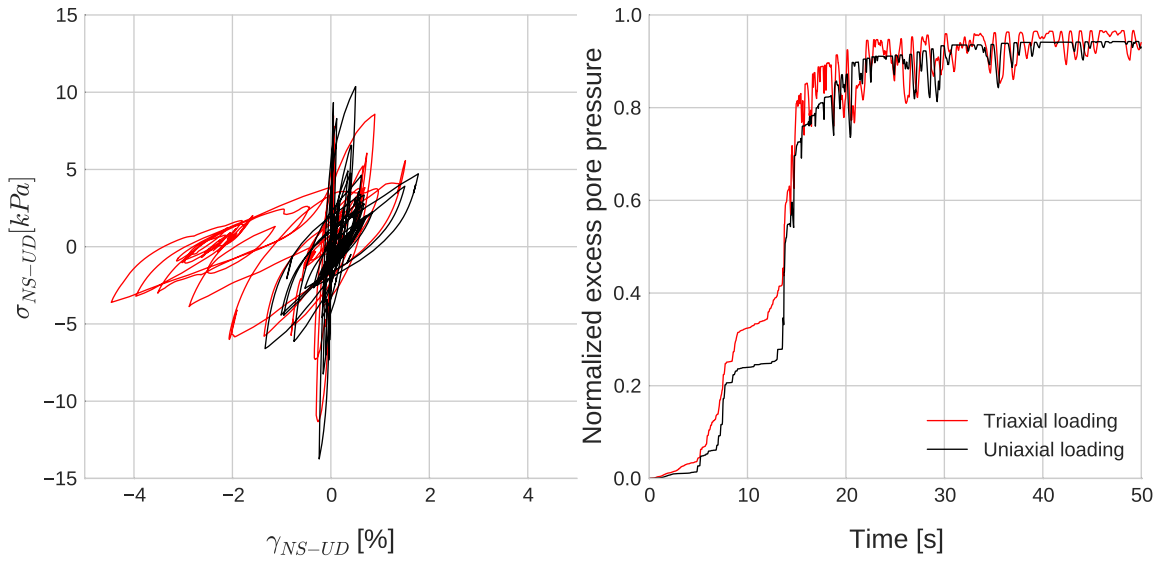

Figure 18: **(a) Comparison of stress-strain curves between uniaxial (in black) and triaxial (in red) loading conditions for NS-UD components at GL-4.0 m; (b) Comparison of pore-pressure ratios at same depth.**

6 Conclusions

This study shows the possibility of modeling wave propagation on nonlinear media including pore-pressure effects using SEM by coupling two different mechanisms. First, the nonlinear soil behavior and second, the excess of pore pressure generation. These models need three elastic parameters (pressure and shear wave velocities and density), three parameters for viscoelastic attenuation (quality factors of P and S waves and reference frequency) and three parameters for nonlinearity (friction angle, cohesion and coefficient of Earth at rest). When excess-pore pressure development is taken into account, five parameters are required (ϕ_p, w_1, p_1, p_2 and S_1), which can be obtained by laboratory tests or strong motion inversion analyses.

The analyses of the 1987 Superstition Hills earthquake (M_L 6.6) data, recorded at the Wildlife Refuge Liquefaction Array (WRLA), show:

- Spiky behavior of the recorded accelerograms is well reproduced by modeling the dilatant soil behavior and related pore-pressure effect.

- Nonlinear computation of the ground motion with no pore-pressure effects still overestimates high-frequency motion and underestimates amplification of low frequencies.

- Triaxial loading conditions result in higher soil nonlinearity, which in turn produces a more rapid rise of the pore-pressure excess. Yet, deformations at depth in materials susceptible to excess-pore pressure generation could be quite large. For this reason, consideration of multi-axial interaction might sometimes be required for a realistic

modeling of seismic wave propagation.

We have seen that this relatively simple model captures most of the physics observed in dilatant soils. This numerical tool is efficient and useful for a better understanding of the influence of soil-related phenomena on 1D seismic wave propagation and multi-axial loading effects. Yet, solid-liquid phase interaction and fluid dissipation cannot be modeled. This aspect deserves further research in the future.

Acknowledgments

The authors would like to thank to Diego Mercerat, Aneta Richterova, Viet Anh Pham, Luca Lenti and Maria Paola Santisi d'Avila for their helpful comments and contributions and to Professor Susumi Iai for his instructive suggestions to the development of our work and this material when coupling the 3D nonlinear model to his 3D liquefaction front model. We would like to acknowledge Jean Paul Ampuero for both his careful review of this work and his preliminary collaboration with one of the co-authors (Luis Fabián Bonilla) that demonstrated that SEM could handle nonlinear wave propagation. We are also grateful to the anonymous reviewer and the editor Professor Jörg Renner for their constructive comments that helped us to improve this paper.

References

Aguirre, J. & Irikura, K. (1997), 'Nonlinearity, liquefaction, and velocity variation of soft soil layers in port island, kobe, during the hyogo-ken nanbu earthquake', *Bulletin of the Seismological Society of America* **87**, 1244–1258.

Aki, K. & Richards, P. G. (2002), *Quantitative seismology*, University Science Books.

Ampuero, J.-P. (2002), Etude physique et numérique de la nucléation des séismes, PhD thesis, Paris 7.

Assimaki, D., Li, W. & Kalos, A. (2011), 'A wavelet-based seismogram inversion algorithm for the in-situ characterization', *Pure and applied geophysics* **168**(10), 1669–1691.

Bardet, J. P. (2000), *EERA: a computer program for equivalent–linear earthquake site response analyses of layered soil deposits*, Department of Civil Engineering, University of Southern California, Los Angeles, CA, 37 pp.

Beyreuther, M., Barsch, R., Krischer, L., Megies, T., Behr, Y. & Wassermann, J. (2010), 'Obspy: A python toolbox for seismology', *Seismological Research Letters* **81**(3), 530–533.

Bielak, J., Ghattas, O. & Kim, E. (2005), 'Parallel octree-based finite element method for large-scale earthquake ground motion simulation', *Computer Modeling in Engineering and Sciences* **10**(2), 99–112.

Bonilla, L. F., Archuleta, R. J. & Lavallée (2005), 'Hysteretic and dilatant behavior of cohesionless soils and their effects on nonlinear site response: Field data observations and modeling', *Bulletin of the Seismological Society of America* **95**(6), 2373–2395.

Bonilla, L. F., Tsuda, K., Régnier, J. & Laurendeau, A. (2011), 'Nonlinear site response evidence of k-net and kik-net records from the 2011 off the pacific coast of tohoku earthquake', *Earth, Planets and Space* **63**(7), 785–789.

Borja, R. I., Duvernay, B. G. & Lin, C.-H. (2002), 'Ground response in lotung: total stress analyses and parametric studies', *Journal of Geotechnical and Geoenvironmental Engineering* **128**(1), 54–63.

Dafalias, Y. F. & Popov, E. P. (1977), 'Cyclic loading for materials with a vanishing elastic region', *Nuclear Engineering and Design* **41**(2), 293–302.

Darendeli, M. B. (2001), Development of a new family of normalized modulus reduction and material damping curves, PhD thesis, The University of Texas at Austin.

Day, S. M. & Bradley, C. R. (2001), 'Memory-efficient simulation of anelastic wave propagation', *Bulletin of the Seismological Society of America* **91**(3), 520–531.

Day, S. M. & Minster, J. B. (1984), 'Numerical simulation of attenuated wavefields using a padé approximant method', *Geophysical Journal International* **78**(1), 105–118.

De Basabe, J. D. & Sen, M. K. (2007), 'Grid dispersion and stability criteria of some common finite-element methods for acoustic and elastic wave equations', *Geophysics* **72**(6), T81–T95.

De Martin, F. (2010), Influence of the nonlinear behavior of soft soils on strong ground motions, PhD thesis, Ecole Centrale Paris.

De Martin, F., Modaressi, H. & Aochi, H. (2007), Coupling of fdm and fem in seismic wave propagation, *in* 'in Proc. of 4th International Conference on Earthquake Geotechnical Engineering, Jun 2007, Greece.'.

Delavaud, E. (2007), Simulation numérique de la propagation d'ondes en milieu géologique complexe: application à l'évaluation de la réponse sismique du bassin de Caracas (Venezuela), PhD thesis, Institut de Physique du Globe de Paris.

Delcourte, S., Fezoui, L. & Glinsky-Olivier, N. (2009), 'A high-order discontinuous galerkin method for the seismic wave propagation', *EDP Sciences* **ESAIM: Proceedings,27**, 70–89.

Di Prisco, C., Stupazzini, M. & Zambelli, C. (2007), 'Nonlinear sem numerical analyses of dry dense sand specimens under rapid and dynamic loading', *International Journal for Numerical and Analytical Methods in Geomechanics* **31**(6), 757–788.

Ducellier, A. & Aochi, H. (2012), 'Interactions between topographic irregularities and seismic ground motion investigated using a hybrid fd-fe method', *Bulletin of Earthquake Engineering* **10**(3), 773–792.

Electric Power Research Institute, E. (1993), Guidelines for determining design basis ground motions, Technical report, Electric Power Reasearch Institute Technological Report EPRI TR-102293.

Emmerich, H. & Korn, M. (1987), 'Incorporation of attenuation into time-domain computations of seismic wave fields', *Geophysics* **52**(9), 1252–1264.

Etienne, V., Chaljub, E., Virieux, J. & Glinsky, N. (2010), 'An hp-adaptive discontinuous galerkin finite-element method for 3-d elastic wave modelling', *Geophysical Journal International* **183**(2), 941–962.

Faccioli, E., Maggio, F., Paolucci, R. & Quarteroni, A. (1997), '2d and 3d elastic wave propagation by a pseudo-spectral domain decomposition method', *Journal of Seismology* **1**(3), 237–251.

Festa, G. & Vilotte, J. P. (2005), 'The newmark scheme as velocity–stress time-staggering: an efficient pml implementation for spectral element simulations of elastodynamics', *Geophysical Journal International* **161**(3), 789–812.

Field, E. H., Zeng, Y., Johnson, P. A. & Beresnev, I. A. (1997), 'Nonlinear sediment response during the 1994 northridge earthquake: Observations and finite source simulations', *Journal of Geophsyical Research* **103(B11)**, 26869–26883, doi:10.1029/98JB02235.

Fung, Y.-c. (1965), *Foundations of solid mechanics*, Prentice Hall.

Gabriel, A.-A., Ampuero, J.-P., Dalguer, L. & Mai, P. M. (2013), 'Source properties of dynamic rupture pulses with off-fault plasticity', *Journal of Geophysical Research: Solid Earth* **118**(8), 4117–4126.

Gandomzadeh, A. (2011), Dynamical soil-structure interactions: Influence of soil behaviour nonlinearities, PhD thesis, Université Paris-Est.

Gélis, C. & Bonilla, L. F. (2012), '2-dp–sv numerical study of soil–source interaction in a nonlinear basin', *Geophysical Journal International* **191**(3), 1374–1390.

Gélis, C. & Bonilla, L. F. (2014), 'Influence of a sedimentary basin infilling description on the 2-dp–sv wave propagation using linear and non-linear constitutive models', *Geophysical Journal International* **198**(3), 1684–1700.

Graves, R. W. (1993), 'Modeling three-dimensional site response effects in the marina district basin, san francisco, california', *Bulletin of the Seismological Society of America* **83**, 1042–1063.

Graves, R. W. (1996), 'Simulating seismic wave propagation in 3d elastic media using staggered-grid finite differences', *Bulletin of the Seismological Society of America* **86**(4), 1091–1106.

Hardin, B. O. & Drnevich, V. P. (1972), 'Shear modulus and damping in soils: measurement and parameter effects', *Journal of Soil Mechanics and Foundations Div* **98**(sm6).

Hartzell, S., Bonilla, L. F. & Williams, R. A. (2004), 'Prediction of nonlinear soil effects', *Bulletin of the Seismological Society of America* **94**(5), 1609–1629.

Hashash, Y. M. & Park, D. (2001), 'Non-linear one-dimensional seismic ground motion propagation in the mississippi embayment', *Engineering Geology* **62**(1), 185–206.

He, C.-H., Wang, J.-T. & Zhang, C.-H. (2016), 'Nonlinear spectral-element method for 3d seismic-wave propagation', *Bulletin of the Seismological Society of America* .

Hinton, E., Rock, T. & Zienkiewicz, O. (1976), 'A note on mass lumping and related processes in the finite element method', *Earthquake Engineering & Structural Dynamics* **4**(3), 245–249.

Holzer, T. L. & Youd, T. L. (2007), 'Liquefaction, ground oscillation, and soil deformation at the wildlife array, california', *Bulletin of the Seismological Society of America* **97**(3), 961–976.

Holzer, T. L., Youd, T. L. & Hanks, T. C. (1989), 'Dynamics of liquefaction during the 1987 superstition hills, california earthquake', *Science* **244**(4900), 56–59.

Iai, S., Matsunaga, Y. & Kameoka, T. (1990), 'Strain space plasticity model for cyclic mobility', *Report of the port and harbour research institute* **29**, 57–83.

Iai, S., Morita, T., Kameoka, T., Matsunaga, Y. & Abiko, K. (1995), 'Response of a dense sand deposit during 1993 kushiro-oki earthquake', *Soils and Foundations* **35**(1), 115–131.

Ishibashi, M. P. & Zhang, X. (1993), 'Unified dynamic shear moduli and damping patios of sand and clay', *Soils and Foundations* **33**(1), 182–191.

Ishihara, K. (1996), *Soil behaviour in earthquake geotechnics*, Clarendon Press.

Iwan, W. D. (1967), 'On a class of models for the yielding behavior of continuous and composite systems', *Journal of Applied Mechanics* **34**(3), 612–617.

Joyner, W. B. (1975), 'A method for calculating nonlinear seismic response in two dimensions', *Bulletin of the Seismological Society of America* **65**(5), 1337–1357.

Joyner, W. B. & Chen, A. T. (1975), 'Calculation of nonlinear ground response in earthquakes', *Bulletin of the Seismological Society of America* **65**(5), 1315–1336.

Kaklamanos, J., Baise, L. G., Thompson, E. M. & Dorfmann, L. (2015), 'Comparison of 1d linear, equivalent-linear, and nonlinear site response models at six kik-net validation sites', *Soil Dynamics and Earthquake Engineering* **69**, 207–219.

Käser, M. & Dumbser, M. (2006), 'An arbitrary high-order discontinuous galerkin method for elastic waves on unstructured meshes—i. the two-dimensional isotropic case with external source terms', *Geophysical Journal International* **166**(2), 855–877.

Kausel, E. & Assimaki, D. (2002), 'Seismic simulation of inelastic soils via frequency-dependent moduli and damping', *Journal of Engineering Mechanics* **128**(1), 34–47.

Kokusho, T. (2004), 'Nonlinear site response and strain-dependent soil properties', *Current science* **87**, 1363–1369.

Komatitsch, D. & Vilotte, J. P. (1998), 'The spectral element method: An efficient tool to simulate the seismic response of 2d and 3d geological structures', *Bulletin of the seismological society of America* **88**(2), 368–392.

Kramer, S. L. (1996), *Geotechnical Earthquake Engineering*, Prentice Hall, Inc., Upper Saddle River, New Jersey.

Kristeková, M., Kristek, J., Moczo, P. & Day, S. M. (2006), 'Misfit criteria for quantitative comparison of seismograms', *Bulletin of the seismological Society of America* **96**(5), 1836–1850.

Laurendeau, A., Perrault, A., Mercerat, D., Bonilla, L. F., Courboulex, F., Beauval, C., Barros, J. G., Vasconez, F., Marinière, J., Singaucho, J. C., Ruiz, M., Alvarado, A. & Bertand, E. (2016), Preliminary observations of site effects during the mw 7.8 pedernales (ecuador) earthquake of april 16th 2016, *in* '5th IASPEI / IAEE International Symposium: Effects of Surface Geology on Seismic Motion August 15-17, 2016, Taipei, Taiwan'.

Lee, M. K. W. & Finn, W. D. L. (1978), *Dynamic effective stress response analysis of soil deposits with energy transmitting boundary including assessment of liquefaction potential*, University of British Columbia, Faculty of Applied Science.

Leroy, Y. M. (2011), *Introduction to the Finite-Element Method for Elastic and Elasto-Plastic Solids*, Springer Vienna, Vienna, pp. 157–239.

Levander, A. R. (1988), 'Fourth-order finite-difference p-sv seismograms', *Geophysics* **53**(11), 1425–1436.

Liu, P. & Archuleta, R. J. (2006), 'Efficient modeling of q for 3d numerical simulation of wave propagation', *Bulletin of the Seismological Society of America* **96**(4A), 1352–1358.

Lyakhovsky, V. & Hamiel, Y. (2009), Nonlinear elasticity and scalar damage rheology model for fractured rocks, *in* 'Meso-Scale Shear Physics in Earthquake and Landslide Mechanics', CRC Press, pp. 123–132.

Lysmer, J. & Drake, L. A. (1972), 'A finite element method for seismology', *Methods in computational physics* **11**, 181–216.

Madariaga, R. (1976), 'Dynamics of an expanding circular fault', *Bulletin of the Seismological Society of America* **66**(3), 639–666.

Marfurt, K. J. & Kurt, J. (1984), 'Accuracy of finite-difference and finite-element modeling of the scalar and elastic wave equations', *Geophysics* **49**(5), 533–549.

Martino, S., Lenti, L., Gélis, C., Giacomi, A. C., Santisi d'Avila, M. P., Bonilla, L. F., Bozzano, F. & Semblat, J. F. (2015), 'Influence of lateral heterogeneities on strong-motion shear strains: Simulations in the historical center of rome (italy)', *Bulletin of the Seismological Society of America* **105**(5), 2604–2624.

Mercerat, E. D., Bonilla, F., Chabot, S., Martin, F. D., Delavaud, E., Gélis, C., Glinsky, N., Kristek, J., Lenti, L., Moczo, P., Oral, E., Richterova, A. & d'Avila, M. P. S. (2016), Modeling of 1d wave propagation in nonlinear soils using the elasto-plastic iwan model by four numerical schemes, *in* '5th IASPEI / IAEE International Symposium: Effects of Surface Geology on Seismic Motion August 15-17, 2016, Taipei, Taiwan'.

Mercerat, E. D. & Glinsky, N. (2015), A nodal discontinuous galerkin method for non-linear soil dynamics, *in* '6th International Conference on Earthquake Geotechnical Engineering 1-4 November 2015 Christchurch, New Zealand'.

Mercerat, E. D., Vilotte, J. P. & Sánchez-Sesma, F. J. (2006), 'Triangular spectral element simulation of two-dimensional elastic wave propagation using unstructured triangular grids', *Geophysical Journal International* **166**(2), 679–698.

Moczo, P. & Kristek, J. (2005), 'On the rheological models used for time-domain methods of seismic wave propagation', *Geophysical Research Letters* **32**(1).

Moczo, P., Kristek, J., Vavrycuk, V., Archuleta, R. J. & Halada, L. (2002), '3d heterogeneous staggered-grid finite-difference modeling of seismic motion with volume harmonic and arithmetic averaging of elastic moduli and densities', *Wave motion* **92**(8), 3042–3066.

Moczo, P., Labák, P., Kristek, J. & Hron, F. (1996), 'Amplification and differential motion due to an antiplane 2d resonance in the sediment valleys embedded in a layer over the half-space', *Bulletin of the Seismological Society of America* **86**, 1434–1446.

Mroz, Z. (1967), 'On the description of anisotropic workhardening', *Journal of the Mechanics and Physics of Solids* **15**(3), 163–175.

Mullen, R. & Belytschko, T. (1982), 'Dispersion analysis of finite element semidiscretizations of the two-dimensional wave equation', *International Journal for Numerical Methods in Engineering* **18**(1), 11–29.

Olsen, K. B. & Archuleta, R. (1996), 'Three-dimensional simulation of earthquakes on the los angeles fault system', *Bulletin of the Seismological Society of America* **86**, 575–596.

Pavlenko, O. V. & Irikura, K. (2003), 'Nonlinear behavior of soils revealed from the records of the 2000 tottori, japan, earthquake at stations of the digital strong-motion network kik-net', *Bulletin of the Seismological Society of America* **96**, 2131–2145.

Peyrusse, F., Glinsky, N., Gélis, C. & Lanteri, S. (2014), A high-order discontinuous galerkin method for viscoelastic wave propagation, *in* 'Spectral and High Order Methods for Partial Differential Equations-ICOSAHOM 2012', Springer, pp. 361–371.

Pham, V. A. (2013), Effets de la pression interstitielle sur la reponse sismique des sols : modélisation numérique 1D/ 3 composantes, PhD thesis, Université Paris-Est.

Prévost, J. H. (1977), 'Mathematical modelling of monotonic and cyclic undrained clay behaviour', *International Journal for Numerical and Analytical Methods in Geomechanics* **1**(2), 195–216.

Pyke, R. M. (2000), 'Tess: A computer program for nonlinear ground response analyses', *TAGA Engineering Systems and Software, Lafayette, California* .

Rajaure, S., Asimaki, D., Thompson, E., Hough, S., Martin, S., Ampuero, J., Dhital, M., Inbal, A., Takai, N., Shigefuji, M. et al. (2016), 'Characterizing the kathmandu valley sediment response through strong motion recordings of the 2015 gorkha earthquake sequence', *Tectonophysics* .

Régnier, J., Bonilla, L., Bard, P., Bertrand, E., Hollender, F., Kawase, H., Sicillia, D., Marot, M., Assimaki, D., Amorosi, A., Boldini, D., Chiaradonna, A., Martin, F. D., Ebrille, M., Falcone, G., Foerster, E., Foti, S., Gélis, C., Gazetas, G., Gingery, J., Glinsky, N., Harmon, J., Hashash, Y., Iai, S., Jeremic, B., Kramer, S., Kontoe, S., Kristek, J., Lanzo, G., di Lernia, A., Lopez-Caballero, F., Mercerat, E. D., Moczo, P., Montoya-Noguera, S., Musgrove, M., Nieto-Ferro, A., Pagliaroli, A., Pisano, F., Richterova, A., Sajana, S., d'Avila, M. S., Shi, J., Silvestri, F., Tropeano, G., Vernucci, L., Wanabe, K., Chen, L., Ghofrani, A. & McAllister, G. (2016), 'International benchmark on numerical simulations for 1d, non-linear site response (prenolin): verification phase based on canonical cases', *Bulletin of the Seismological Society of America, under revision* .

Roten, D., Fäh, D. & Bonilla, L. F. (2013), 'High-frequency ground motion amplification during the 2011 tohoku earthquake explained by soil dilatancy', *Geophysical Journal International* **193**(2), 898–904.

Roten, D., Fäh, D. & Bonilla, L. F. (2014), 'Quantification of cyclic mobility parameters in liquefiable soils from inversion of vertical array records', *Bulletin of the Seismological Society of America* **104**(6), 3115–3138.

Roumelioti, Z. & Beresnev, I. A. (2003), 'Stochastic finite-fault modeling of ground motions from the 1999 chi-chi, taiwan, earthquake: Application to rock and soil sites with implications for nonlinear site response', *Bulletin of the Seismological Society of America* **93**, 1691–1702.

Saenger, E. H., Gold, N. & Shapiro, S. A. (2000), 'Modeling the propagation of elastic waves using a modified finite-difference grid', *Wave motion* **31**(1), 77–92.

Santisi d'Avila, M. P., Lenti, L. & Semblat, J. F. (2012), 'Modelling strong seismic ground motion: three-dimensional loading path versus wavefield polarization', *Geophysical Journal International* **190**(3), 1607–1624.

Schnabel, B., Lysmer, J. & Seed, H. B. (1972), *Shake. A computer Program for Earthquake Response Analysis of Horizontally Layered Sites*, College of Engineering, University of Berkeley, CA. Rep., No. EERC.

Seed, H. B. & Idriss, I. M. (1969), 'Influence of soil conditions on ground motions during earthquakes', *Journal of the Soil Mechanics and Foundations Division* **95**(1), 99–138.

Seriani, G. (1998), '3-d large-scale wave propagation modeling by spectral element method on cray t3e multiprocessor', *Computer Methods in Applied Mechanics and Engineering* **164**(1), 235–247.

Seriani, G. & Priolo, E. (1991), High-order spectral element method for acoustic wave modeling, *in* '1991 SEG Annual Meeting', Society of Exploration Geophysicists.

Smerzini, C., Paolucci, R. & Stupazzini, M. (2011), 'Comparison of 3d, 2d and 1d numerical approaches to predict long period earthquake ground motion in the gubbio plain, central italy', *Bulletin of Earthquake Engineering* **9**(6), 2007–2029.

Stewart, J. P. & Kwok, A. O. (2008), Nonlinear seismic ground response analysis: Code usage protocols and verification against vertical array data, *in* 'Geotechnical earthquake engineering and soil dynamics IV', ASCE Geotechnical Special Publication, pp. 1–24.

Stupazzini, M., Paolucci, R. & Igel, H. (2009), 'Near-fault earthquake ground-motion simulation in the grenoble valley by a high-performance spectral element code', *Bulletin of the Seismological Society of America* **99**(1), 286–301.

Stupazzini, M. & Zambelli, C. (2005), 'Geo-elsevp: a spectral element approach for 2d or 3d dynamic elasto-viscoplastic problems', *Rivista Italiana di Geotecnica* **39**(4), 70–82.

Thomas, M. Y., Bhat, H. S., & Klinger, Y. (2017), 'Dynamic off-fault damage and seismic radiation, in "fault zone properties and processes during dynamic rupture"'.

Towhata, I. & Ishihara, K. (1985), Modelling soil behavior under principal stress axes rotation, *in* 'International conference on numerical methods in geomechanics', pp. 523–530.

Virieux, J. (1986), 'P-sv wave propagation in heterogeneous media: velocity-stress finite-difference method', *Geophysics* **51**, 889–901.

Vucetic, M. & Dobry, R. (1991), 'Effect of soil plasticity on cyclic response', *Journal of geotechnical engineering* **117**(1), 89–107.

Wang, Z. L., Dafalias, Y. F. & Shen, C. K. (1990), 'Bounding surface hypoplasticity model for sand', *Journal of engineering mechanics* **116**(5), 983–1001.

Xu, S., Ben-Zion, Y. & Ampuero, J.-P. (2012), 'Properties of inelastic yielding zones generated by in-plane dynamic ruptures—i. model description and basic results', *Geophysical Journal International* **191**(3), 1325–1342.

Xu, S., Ben-Zion, Y., Ampuero, J.-P. & Lyakhovsky, V. (2015), 'Dynamic ruptures on a frictional interface with off-fault brittle damage: feedback mechanisms and effects on slip and near-fault motion', *Pure and Applied Geophysics* **172**(5), 1243–1267.

Yoshida, N. & Iai, S. (1998), 'Nonlinear site response and its evaluation and prediction', *in Proc. of Second International Symposium on the Effects of Surface Geology on Seismic Motion, K. Irikura, K. Kudo, H. Okada, and T. Sasatani (Editors)* **1**, 71–90.

Appendix A.

The spectral element method scheme relates the strain and stress parameters for each GLL point of grid element. To do so, we follow the MPII formulation of Iwan's model (1967). In this section, the equations of MPII model are first presented and the constitutive model for the liquefaction front is then detailed.

A.1 Iwan model

We follow Joyner's formulation (1975) of Iwan's model (1967). Three-dimensional model of nonlinearity is presented based on standard incremental plasticity theory of Fung (1965) by introducing a family of yield surfaces. In his formulation, yield surfaces are expressed by the following formula:

$$F_n(s_{ij} - \alpha_{nij}) = k_n^2 \tag{A.1}$$

where F_n is the yield function for the n^{th} yield surface, α_{nij} is its origin and k_n is the yield stress associated to each n^{th} surface. The translation for each surface due to kinematic hardening of Prager type can be written in terms of plastic strain, as shown in Equation A.2, where C_n is a constant for the n^{th} surface.

$$d\alpha_{nij} = C_n de_{pnij} \tag{A.2}$$

$$de_{pnij} = L_n h_n \frac{\partial F_n}{\partial s_{ij}} \tag{A.3}$$

Fung (1965) states that an incremental loading of ds_{rs} from a plastic state must lead to another plastic state. Normality condition described by Equation A.3 is then used to compute h_n as follows:

$$h_n = \frac{1}{C_n} \frac{(\partial F_n/\partial s_{rs})ds_{rs}}{(\partial F_n/\partial s_{kl})(\partial F_n/\partial s_{kl})} \tag{A.4}$$

For the case when the yield function does not exceed k_n value or unloading, L_n parameter is set to zero, while for other cases it is equal to 1.

$$L_n = 0 \text{ if } F_n < k_n^2 \text{ or } \frac{\partial F_n}{\partial s_{ij}} ds_{ij} < 0$$

$$L_n = 1 \text{ if } F_n = k_n^2 \text{ or } \frac{\partial F_n}{\partial s_{ij}} ds_{ij} \geq 0$$

In case of yielding ($L_n = 1$), the n^{th} surface is considered to be activated.

For a given strain increment $d\epsilon_{ij}$, the corresponding stress increment $d\sigma_{ij}$ is calculated using the deviatoric strains de_{ij} and stresses ds_{ij}. The total deviatoric strain increment de_{ij} can be obtained by the strain increment $d\epsilon_{ij}$ as in Equation A.5. In this case, *total* stands for the sum of the elastic and plastic strains.

$$de_{ij} = d\epsilon_{ij} + d\epsilon_m \delta_{ij} \tag{A.5}$$

where $d\epsilon_m$ is the mean strain increment written as $d\epsilon_m = \frac{1}{3}(tr(d\epsilon))$.

In the constitutive model, the total deviatoric strain increment de_{ij} is related to the deviatoric stress increment ds_{ij} by Equation A.6.

$$de_{ij} = Q_{ijrs} ds_{rs} + 1/2G_0 ds_{ij} \tag{A.6}$$

Q_{ijrs} tensor is calculated cumulatively for each plasticity surface using the corresponding yield function and partial derivatives as in Equation A.7.

$$Q_{ijrs} = \sum_n \frac{L_n(\partial F_n/\partial s_{ij})(\partial F_n/\partial s_{rs})}{C_n(\partial F_n/\partial s_{kl})(\partial F_n/\partial s_{kl})} \tag{A.7}$$

By using Von Mises yielding condition, the yield function F_n and its partial derivative $\partial F_n/\partial s_{ij}$ can be written as follows:

$$F_n = 1/2(s_{nij} - \alpha_{nij})(s_{nij} - \alpha_{nij}) \tag{A.8}$$

$$\frac{\partial F_n}{\partial s_{ij}} = s_{nij} - \alpha_{nij} \tag{A.9}$$

C_n and k_n values are determined following the soil backbone curve. k_n values correspond to the yield stress for each spring; C_n values are then calculated by Equation A.10.

$$\frac{1}{C_j} = \frac{\epsilon_{j+1} - \epsilon j}{k_{j+1} - k_j} - \frac{1}{2G_0} - \sum_{n=1}^{j-1} 1/C_n \tag{A.10}$$

To solve the system of equations, we follow the scheme shown in Figure A.19. At each time step t, total stress increment $d\sigma_{ij}$ is calculated for total strain increment $d\epsilon_{ij}$. For the first time step, we assume that no yield surface is activated and the current stress point remains inside the first plasticity surface. Thus, it is possible to apply linear elasticity to calculate the stress increment of the material for the given strain increment. For the next time steps, the deviatoric strain de_{ij} is computed with Equation A.5. Then, yield function F_n and its partial derivative $\partial F_n/\partial \sigma_{ij}$ are calculated by Equations A.8-A.9. For the current stress state L_n is computed to check whether the n^{th} surface yields. Then, E matrix is created by assembling elastic and plastic multipliers, $1/2G_0$ and Q_{ijrs}, with respect to Equation A.6. This matrix relates the deviatoric stress increment to deviatoric strain increment. To solve Equation A.6, E is inverted and multiplied by the deviatoric strain increment. We assume that the time step is sufficiently small that the solution provides an acceptable approximation. Once, the deviatoric stress increment ds_{ij} is obtained, total deviatoric stress s_{ij} is updated. Then, the translation of the center for each activated yield surface α_{ij} is computed (See Equation A.11). Lastly, the stress increment $d\sigma_{ij}$ can be computed according to Equation A.12.

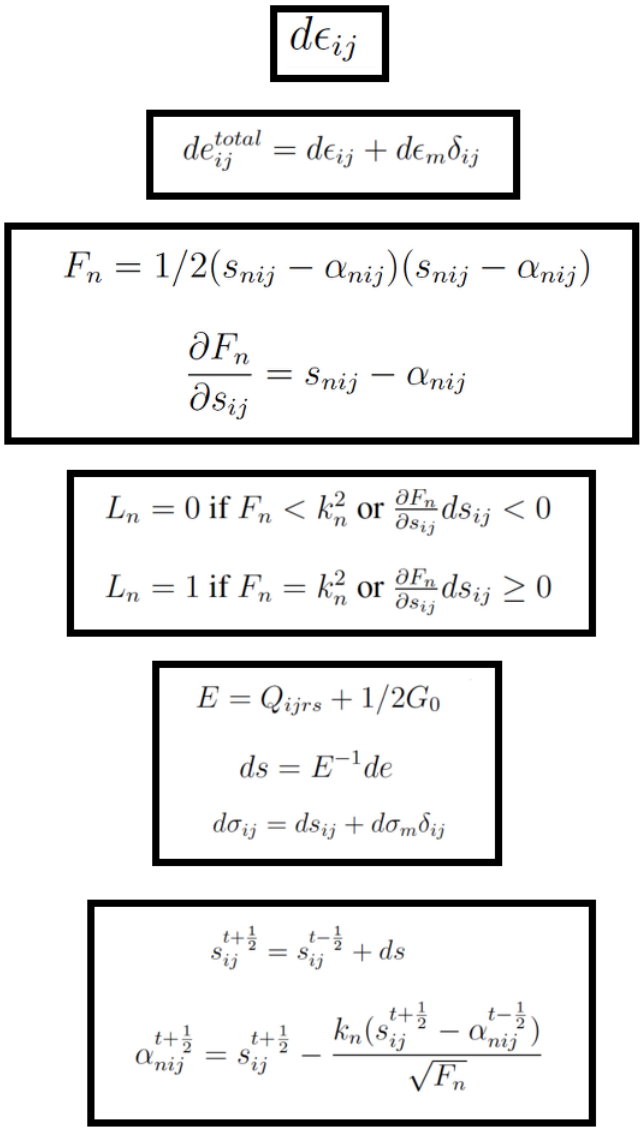

Figure A.19: Numerical flow for computation of total stress increment for given total strain increment.

$$\alpha_{nij}^{t+\frac{1}{2}} = s_{ij}^{t+\frac{1}{2}} - \frac{k_n(s_{ij}^{t+\frac{1}{2}} - \alpha_{nij}^{t-\frac{1}{2}})}{\sqrt{F_n}} \tag{A.11}$$

$$d\sigma_{ij} = ds_{ij} + d\sigma_m \delta_{ij} \tag{A.12}$$

where $t + \frac{1}{2}$ and $t - \frac{1}{2}$ hold for current and previous time step values. $d\sigma_m$ is the mean stress increment and calculated using the mean strain increment $d\epsilon_m$ and bulk modulus K as $d\sigma_m = 3K d\epsilon_m$.

A.2 Liquefaction front model

In Iai et al. (1990) model, the liquefaction front parameter S_0 is determined depending on the cumulative shear work exerted on the soil. This parameter indicates how close the soil is to liquefaction state. In particular, for $S_0 = 0$, liquefaction is assumed to occur. Since we do not model the ultimate state at which liquefaction takes place, we limit its value using the S_1 parameter. Initially, S_0 is set to 1 for cases where initial deviatoric stress ratio is considerably low ($\tau_0/P_0 < 0.67 sin\phi_p$). For higher values of initial deviatoric stress ratio ($\tau_0/P_0 > 0.67 sin\phi_p$), S_0 is obtained solving the second order polynomial in Equation A.13.

$$S = \begin{cases} S_0, & \text{if } r \leq r_3 \\ S_2 + \sqrt{(S_0 - S_2)^2 + (\frac{r - r_3}{sin\phi_f})^2}, & \text{else} \end{cases} \tag{A.13}$$

where r is the normalized deviatoric stress, $r_3 = 0.67 sin\phi_p S_0$, $S_2 = S_0 - \frac{sin\phi_p S_0 - r_3}{sin\phi_f}$, and ϕ_p is the angle of the phase transformation line (Figure A.20).

For liquefiable soil layers, the principal stress σ_p from total stress matrix is computed. Then, the current deviatoric stress is computed by Equation A.14. Plastic shear work increment is calculated by Equation A.15 using deviatoric stress s. In this formulation cumulative plastic shear work is directly calculated from 3D plastic strain increment (Iai, personal communication 2016).

$$\tau = \frac{\sigma_p(max) - \sigma_p(min)}{2} \tag{A.14}$$

$$dW_s{}^p = \sum_{i=1}^{3} \sum_{j=1}^{3} (s_{ij} d\varepsilon_{ij}{}^p) \tag{A.15}$$

During computation of plastic shear work increment, a correction is applied by $dW_s = dW_s Cor$ to ensure a positive plastic shear work increment. Otherwise, the increment is considered to be zero (Equations A.16-A.18).

$$Cor = \begin{cases} 1, & \text{if } \frac{r}{cst} \leq 0.67 sin\phi_p \\ \frac{(sin\phi_f) - \frac{r}{cst}}{sin\phi_f - 0.67 sin\phi_p}, & \text{else} \end{cases} \tag{A.16}$$

$$cst = \begin{cases} 1, & \text{if } S \geq 0.4 + (S_b - 0.4) S_0 / S_b \\ 0.4 + (S_b - 0.4) S_0 / S_b, & \text{else} \end{cases} \tag{A.17}$$

$$S_b = \begin{cases} S_0, & \text{if } S_0 < 0.4 \\ 0.4, & \text{else} \end{cases} \tag{A.18}$$

The increment of plastic shear work dW_s is used to obtain the cumulative plastic shear work W_s. This increment is added to the previous value of cumulative shear work $W_s^{t-\frac{1}{2}}$ such that $W_s = W_s^{t-\frac{1}{2}} + dW_s$. Then, the shear work ratio w is computed as follows:

$$w = W_s/W_n \tag{A.19}$$

$$W_n = \frac{\tau_{max}\gamma_0}{2} \tag{A.20}$$

where W_n is the initial shear work and τ_{max} is the maximum shear strength. Knowing that $\gamma_0 = \frac{\tau_{max}}{G}$ and G, which is the corrected shear modulus (Equation 2), Equation A.20 can be rewritten as:

$$W_n = \frac{(\tau_{max})^2}{2G} \tag{A.21}$$

Using the shear work ratio w, the liquefaction front parameter S_0 is updated by Equation A.22. Therefore, the model parameters are p_1, which controls the initial pore pressure raise up to $S < 0.4$; p_2 controls the pore-pressure evolution during dilatancy; and, w_1 controls the slope of pore-pressure excess (Figure 1).

$$S_0 = \begin{cases} 1 - 0.6(\frac{w}{w_1})^{p_1}, & \text{if } w \leq w_1 \\ (0.4 - S_1)(\frac{w_1}{w})^{p_2} + S_1, & \text{if } w > w_1 \end{cases} \tag{A.22}$$

The normalized mean effective stress S can be calculated by the liquefaction front parameter S_0 following Equation A.13. Finally, the pore-pressure excess can be written in function of initial effective stress P_0 as:

$$u = P_0(1 - S) \tag{A.23}$$

To couple pore pressure effects with MPII model, we reconstruct the backbone curve by using the updated values of the reference strain $\gamma_{ref}^{current}$ and shear modulus $G^{current}$ (Equations A.24-A.26).

$$\gamma_{ref}^{current} = \begin{cases} \gamma_{ref}, & \text{if } S_0 > S_b \\ \gamma_{ref}/(S_0/S_b), & \text{else} \end{cases} \tag{A.24}$$

$$G^{current} = P_0 sin\phi_f S + \Delta \tag{A.25}$$

where Δ corresponds to

$$\Delta = \begin{cases} 0, & \text{if } S_0 > S_b \\ (sin\phi_f - sin\phi_p)(S_b - S_0)(0.4/S_b)P_0, & \text{else} \end{cases} \tag{A.26}$$

The algorithm is shown in Figure A.20.

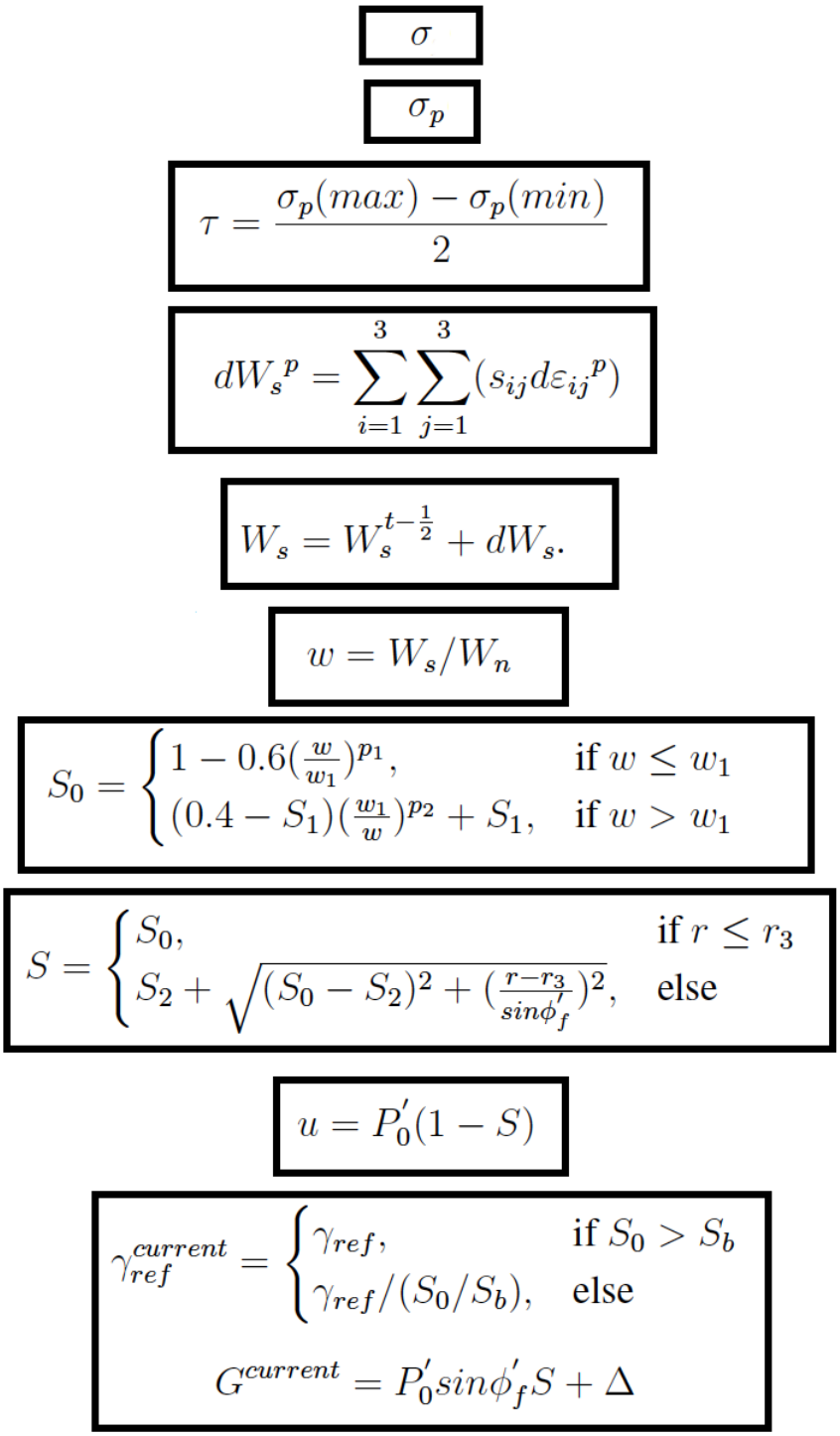

Figure A.20: Numerical flow followed for coupling of pore-pressure effects and MPII model.

Appendix B.

The problem of assessing the accuracy and convergence of SEM when dealing with nonlinear media deserves a further study. We attempt to partially answer this issue by showing some convergence on the computed transfer function varying the number of GLL nodes and the number of springs used to approximate the nonlinear soil behavior. The reference solution is computed using 300 springs and 12 GLL nodes.

The error is computed as the difference between each test and the reference over all the frequency band between 0.1 and 8 Hz (Equation B.1). Where, N_f is the total number of frequency bins.

$$error = \frac{\sum_{i=1}^{N_f} TF_{solution}(i)/TF_{reference}(i)}{N_f} \tag{B.1}$$

Figure B.21 displays the calculated error when using different number of GLL nodes (3, 5, 7, 9) (left) and for different number of Iwan springs (10, 20, 50, 100 and 200) (right). The test uses the P1 soil model (detailed in Section 3). Element size is fixed to 2 m for all models.

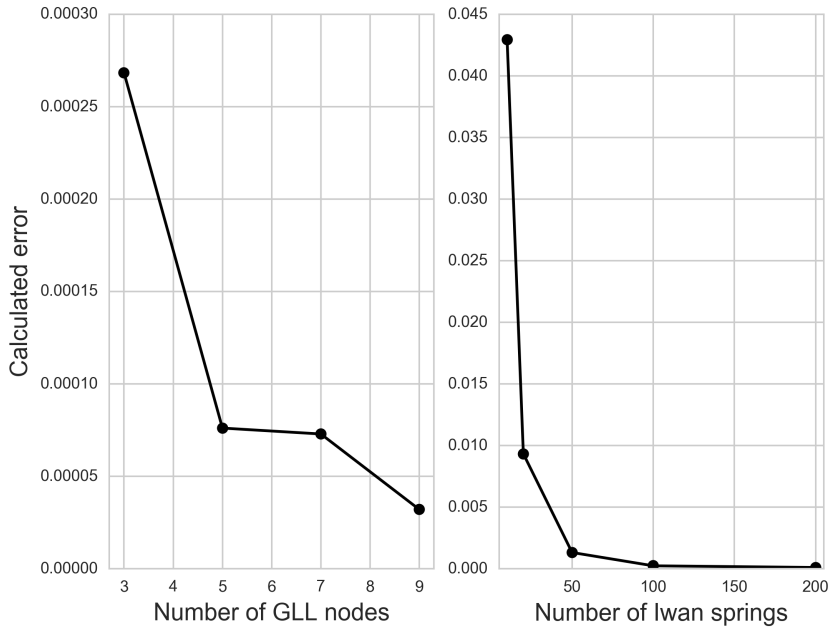

Figure B.21: Calculated error as a function of number of GLL nodes (left); Calculated error as a function of Iwan spring number (right) in P1 model.

The error decreases significantly by increasing the number of GLL from 3 to 5 (4 times reduction). SEM solutions having 5 and 7 GLL nodes do not differ considerably, while using 9 GLL nodes results in further decrease. As for the number of springs, the error when using 10 springs is approximately 5 times higher than the model with 20 springs. The error is further

reduced 7 times for the case of 50 springs (0.1 %). The use of more than 50 springs produces even smaller error values. Based on these results, we decided that the use of 50 springs and 5 GLL nodes defined on each spectral element could provide a fairly optimum solution for this tested example.

Appendix C.

To quantify the goodness-of-fit (GOF) between two time histories, we use the method proposed by Kristekova et al., 2006. The method uses the continuous wavelet transform to evaluate the misfit in a time-frequency representation of the signals. Hence, simultaneous envelope and phase differences in time and frequency are quantified. In particular, we use the method implementation in the Obspy package (Beyreuther et al., 2010) where GOF is computed and a value of 10 means that the two signals are identical. In the following, we show the GOF for the different models computed in this paper.

C.1 Goodness-of-fit for Rome computations

In Figure C.22, velocity-time histories are compared between SEM and HT methods solutions. Figure C.23 displays the GOF computed for these simulations. Note the high GOF values in both envelope (9.95) and phase (9.98).

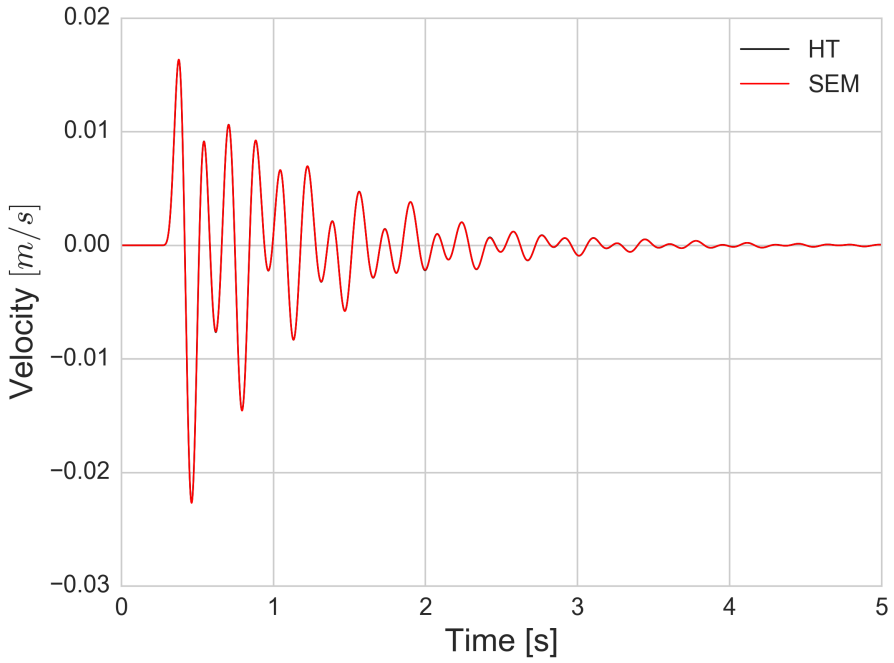

Figure C.22: Comparison between velocity-time histories at surface from SEM (in red) and HT (in black).

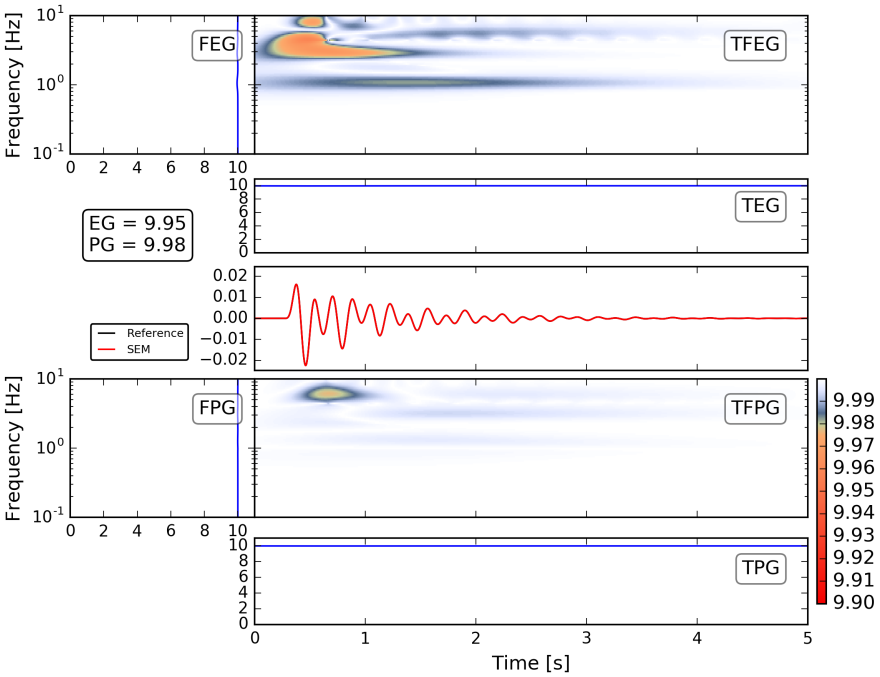

Figure C.23: GOF between the reference signal (HT) and the SEM solution on the computed velocity time histories for Rome model. It is shown the frequency envelope goodness FEG (left), time-frequency envelope goodness TFEG (right), time envelope goodness TEG (middle right) (top) and frequency phase goodness FPG (left), time-frequency phase goodness TFPG (right), and time phase goodness TPG (middle right) (bottom).

C.2 Goodness-of-fit for P1 computations

Figure C.24 shows the GOF of acceleration-time histories for SEM and DGM solutions. Two numerical methods have quite similar results, in particular, there is a very good agreement in phase.

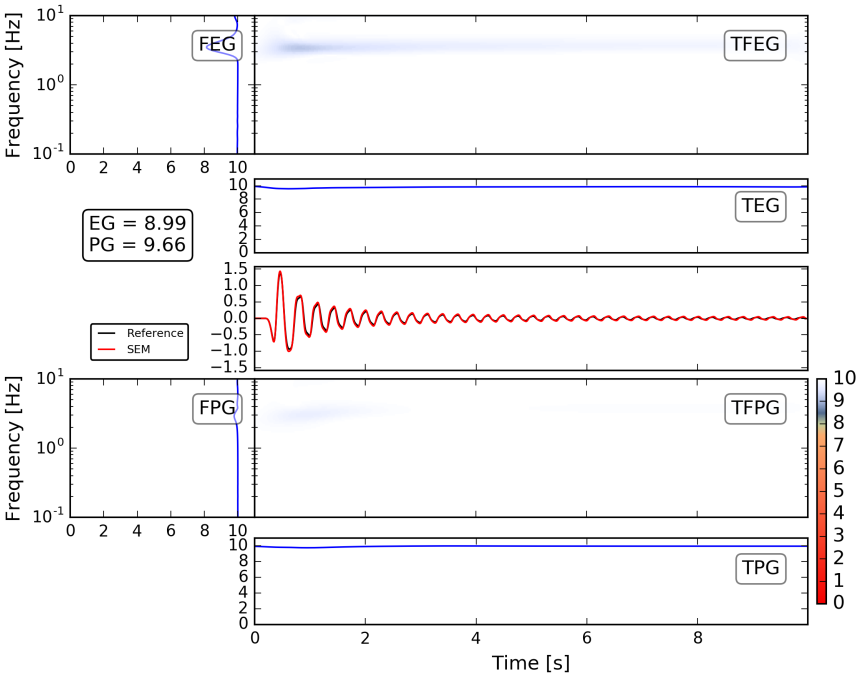

Figure C.24: Same as C.23 for accelerograms computed with SEM and DGM using the P1 soil model.

C.3 Goodness-of-fit for WRLA computations

Acceleration-time histories

Figures C.25-C.27 (EW, NS and vertical directions, respectively) display the GOF of acceleration time histories between SEM solution and observations. SEM solutions are in good agreement in both phase and envelope (GOF ~ 7 for all three components). The best fit is seen for the NS direction. The fit decreases starting at 13 seconds approximately where strong excess-pore pressure build-up is developed. These differences are higher at low frequencies (< 1 Hz). This tendency is observed in all components.

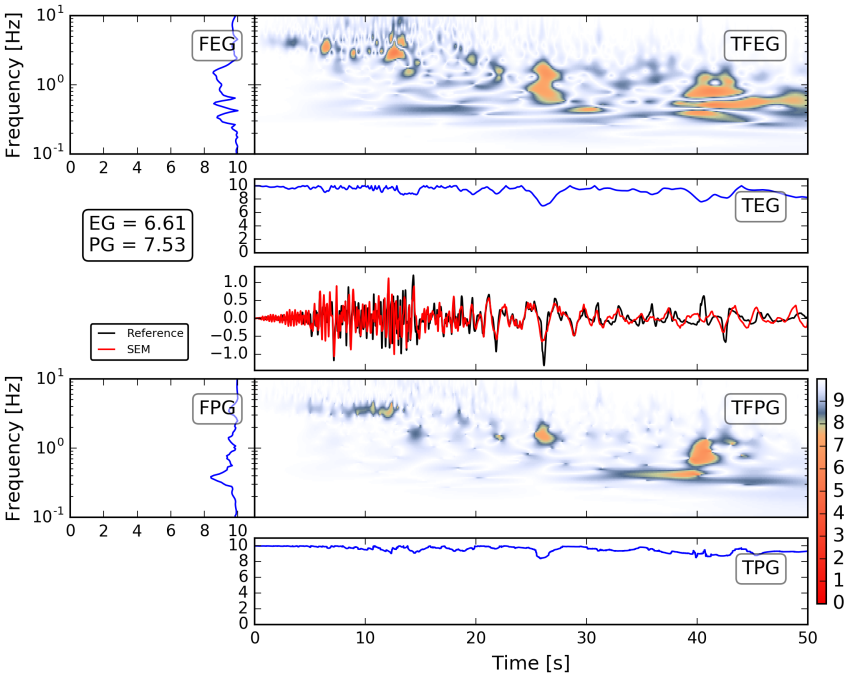

Figure C.25: Same as Figure C.23 for EW component in WRLA soil model.

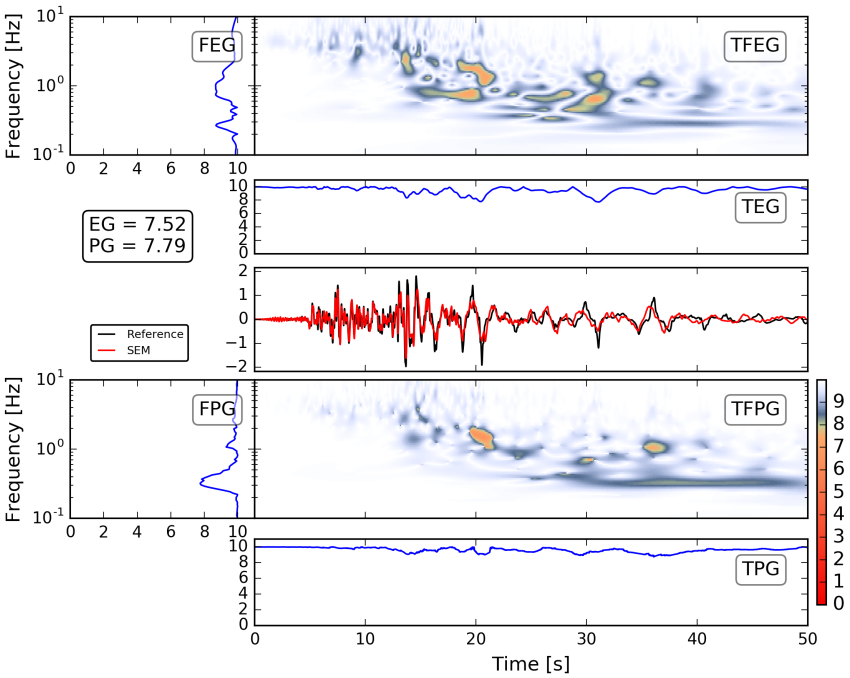

Figure C.26: Same as Figure C.23 for NS component in WRLA soil model

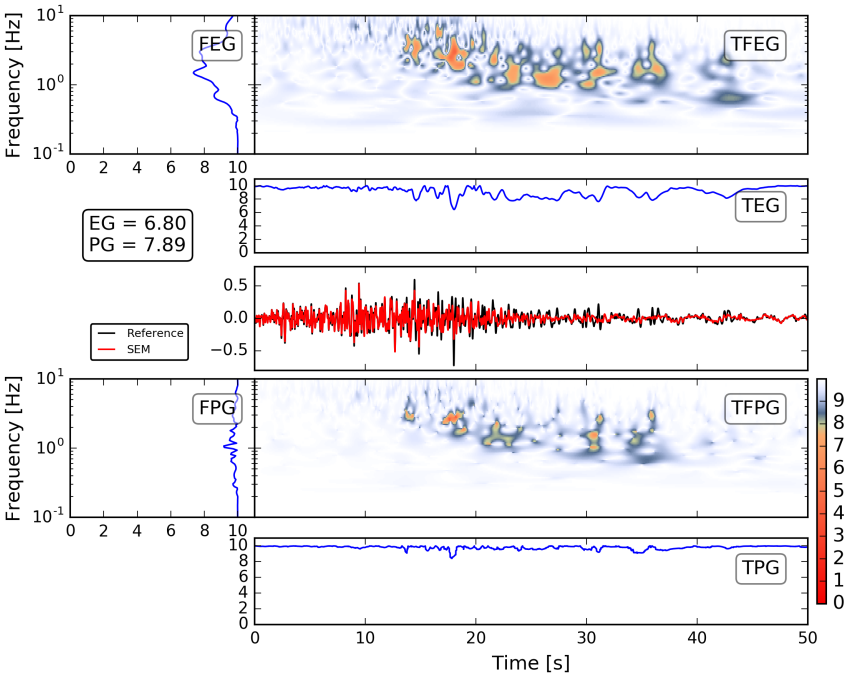

Figure C.27: Same as Figure C.23 for UD component in WRLA soil model

Velocity-time histories

Figures C.28-C.30 display the GOF for EW, NS and UD directions. The differences are more localized, and around 0.3 Hz. Over all, the fit is satisfactory and noticeable differences in phase are observed after 30 s of ground motion.

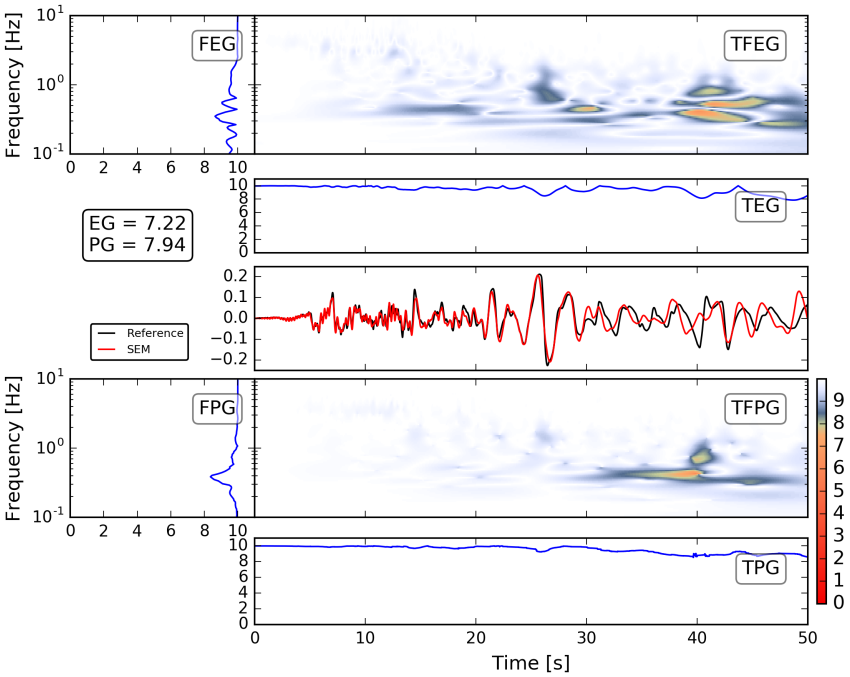

Figure C.28: Same as Figure C.23 for EW component in WRLA soil model

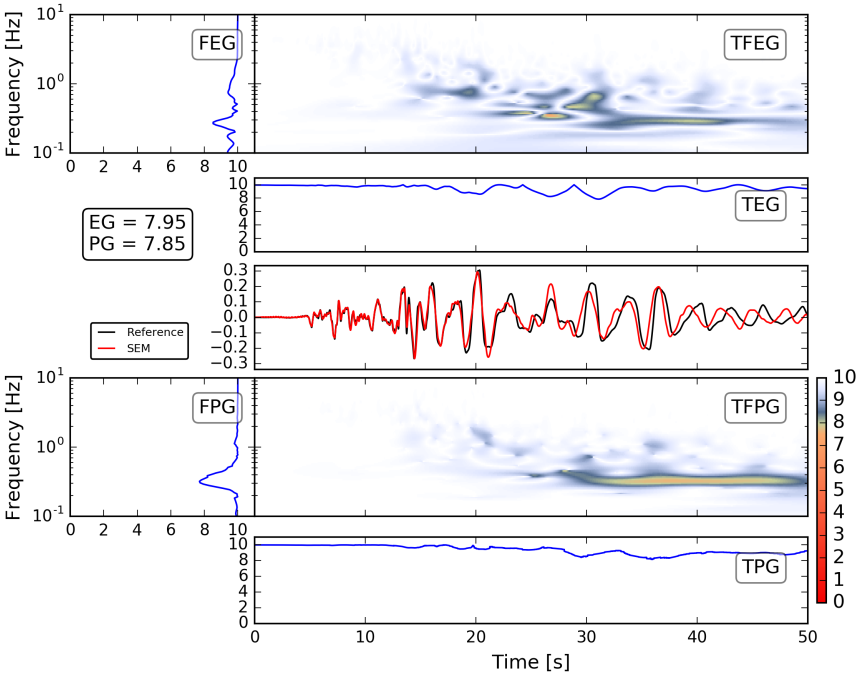

Figure C.29: Same as Figure C.23 for NS component in WRLA soil model

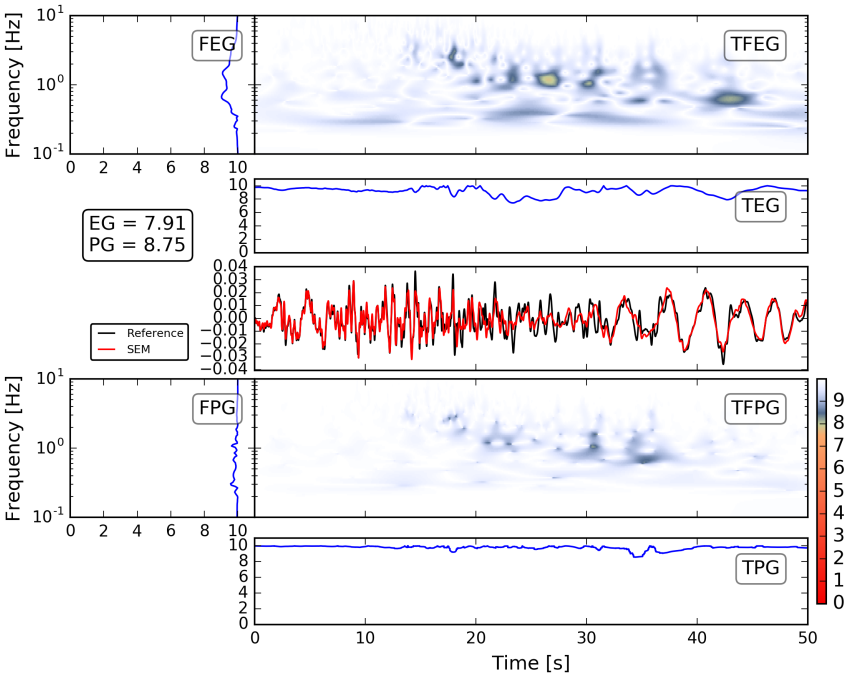

Figure C.30: Same as Figure C.23 for UD component in WRLA soil model